Improving the Heat Transfer Characteristics of the Spiky Central Receiver Air Pre-Heater (SCRAP) using Helically Swirled Fins

by

Dewald Grobbelaar

Thesis presented in partial fulfilment of the requirements for the degree of Master of Engineering (Mechanical) in the Faculty of Engineering at Stellenbosch University

Supervisor: Prof. T.W. Von Backström
Co-supervisor: Dr. M. Lubkoll

April 2019

Declaration

By submitting this thesis electronically, I declare that the entirety of the work contained therein is my own, original work, that I am the sole author thereof (save to the extent explicitly otherwise stated), that reproduction and publication thereof by Stellenbosch University will not infringe any third party rights and that I have not previously in its entirety or in part submitted it for obtaining any qualification.

Date: April 2019

Abstract

Improving the Heat Transfer Characteristics of the Spiky Central Receiver Air Pre-Heater (SCRAP) using Helically Swirled Fins

D. Grobbelaar

Department of Mechanical and Mechatronic Engineering,
University of Stellenbosch,
Private Bag X1, Matieland 7602, South Africa.

Thesis: MEng (Mech)

April 2019

The purpose of this project is to investigate the effect of helically swirled fins on the heat transfer coefficient and pressure drop in the spiky central receiver air pre-heater (SCRAP).

First a theoretical analysis was done to investigate the effects of a swirl on the heat transfer coefficient and pressure drop. After this, the effects of swirled fins were simulated numerically and investigated. Experiments were then conducted to provide validation of the numerical model.

Empirical correlations indicated that there is an increase of 20 % - 30 % in the heat transfer coefficient at low Reynolds numbers ($\mathrm{Re} = 6600$ and $\dot{m} = 0.03\,\mathrm{kg/s}$), while maintaining pressure losses below 20 %. Higher (Re larger than 22 000 and $\dot{m} > 0.1$ kg/s) Reynolds numbers introduced large pressure drops, surpassing a 100 % increase, accompanied by mediocre heat transfer coefficient increases of 34 %.

For the straight duct the average difference between analytical and numerical results was 14.8 % for the heat transfer coefficient and 7.5 % for the pressure drop. The curved duct simulation deviates from the analytical results by 14.3 % for the heat transfer coefficient. For the pressure drop a maximum of 11.2 % deviation is experienced, with a accuracy of 4 % within the region of $5000 < \mathrm{Re} < 27\,500$.

A test section was designed, containing 24 symmetrical helically swirled fins, making one full rotation within 200 mm. Due to its complex geometry the test section was manufactured using selective laser sintering. Tests were then conducted at a constant temperature of a nominally 100 °C on the outside of the section, provided through a steam chamber at ambient pressure. Compressed air then flowed through the inner curved ducts.

An over-prediction of 10 % is experienced in the heat transfer coefficient for the numerical simulation compared to the experimental results. This over-prediction is due to the numerical simulation being an ideal situation with no external factors influencing the outcome. Further for the curved duct, analytical pressure drop predictions, at flow rates of $5000 < \mathrm{Re} < 22\,000$, compared well to both the experimental and numerical results. These results stay within 10 % from each other.

In conclusion, it was found that with the implementation of swirled fins the heat transfer coefficient can be increased with 21 % - 29 %. All the same the pressure drop increases remarkably from 8 %, at 21 % increase in heat transfer coefficient, to almost 300 %, at a heat transfer coefficient increase of 29 %, for the investigated case. The implementation of curved ducts is thus an option at low flow rates where the pressure drop will not be increased greatly.

It was found that with a flow rate of less than 0.035 kg/s the heat transfer coefficient increase will be larger than the pressure drop increase. At the design point, which is 0.0326 kg/s, the heat transfer coefficient increases by 23 % with an increase in pressure drop of 20 %. However, the manufacturing of these complex fins are very expensive, making the implementation of swirled fins challenging.

Uittreksel

Die Verbetering van Warmte-oordrag Eienskappe van die Puntige Sentrale Ontvanger Lug-Voorverwarmer (PSOLV) deur die gebruik van heliese gewentelde vinne

(Improving the Heat Transfer Characteristics of the Spiky Central Receiver Air Pre-Heater (SCRAP) using Helically Swirled Fins)

D. Grobbelaar

Departement Meganiese en Megatroniese Ingenieurswese,
Universiteit van Stellenbosch,
Privaatsak X1, Matieland 7602, Suid Afrika.

Tesis: MIng (Meg)

April 2019

Die doel van hierdie projek is om die effek van helies gekrulde vinne in die puntige sentrale ontvanger lug-voorverwarmer (PSOLV) op die warmte-oordragskoëffisiënt en drukval te ondersoek.

Teoretiese analise was gedoen om die effekte van 'n krul op die warmte-oordragskoëffisiënt en drukval te ondersoek. Daarna is die effekte van gekrulde vinne numeries gesimuleer en ondersoek. Eksperimente was toe uitgevoer om die numeriese model te bevestig.

Die empiriese korrelasies dui 'n 20 % - 30 % toename in warmte-oordragskoëffisiënt, gepaard met aanvaarbare drukverliese van laer as 20 % by lae vloeitempo's ($\mathrm{Re} = 6600$ en $\dot{m} = 0.03$ kg/s). Hoër vloeitempo's ($\mathrm{Re} > 22\,000$ en $\dot{m} > 0.1$ kg/s) lei tot groot druk verliese van groter as 100 %, gepaardgaande met middelmatige verbetering in die warmte-oordragskoëffisiënt van 34 %.

Vir die reguit kanaal was die gemiddelde verskil tussen die teoretiese en simulasie resultate 14,8 % vir die warmte-oordragskoëffisiënt en 7,5 % vir die drukval. Die gekrulde kanaal simulasie verskil van die teoretiese resultate met 14,3 % vir die warmte-oordragskoëffisiënt. Vir die drukval was 'n maksimum van 11,2 % afwyking waargeneem, met 'n akkuraatheid van 4 % binne die vloeistreek van

$5000 < \mathrm{Re} < 27\ 500$.

'n Toets afdeling was ontwerp, wat bestaan uit 24 simmetriese helies gekrulde vinne, wat een volle rotasie binne 200 mm maak. Die toetsafdeling is vervaardig deur selektiewe laser sintering. Hierdie metode was gekies as gevolg van die toetsafdeling se komplekse meetkunde. Toetse was gedoen om so ver as moontlik 'n konstante temperatuur van 100 °C op die buitekant van die toets deel te implementeer en lug dan deur die binne gekrulde kanale te laat vloei.

Die warmte-oordragskoëffisiënt word oorvoorspel met n persentasie van 10 % vir die simulasie in vergelyking met die eksperimentele resultate. Hierdie oorvoorspelling is as gevolg van die simulasie kondisies wat ideaal is en geen eksterne faktore 'n invloed daarop het nie. Verder vir die gekrulde kanaal het die teoretiese drukvalvoorspellings by lae vloeitempo's van $5000 < \mathrm{Re} < 22\,000$, goed vergelyk met beide die eksperimentele en simulasie resultate. Die afwyking tussen hierdie resultate bly binne 10 %.

Ten slotte is dit bevind dat die warmte-oordragskoëffisiënt, met die implementering van gekrulde vinne, met 21 % - 29 % verhoog kan word. Ongelukkig verhoog die drukval geweldig van 8 % (teen 21 % toename in warmte-oordragskoëffisiënt) tot byna 300 % (teen 'n warmte-oordragskoëffisiënt toename van 29 %) vir die spesifieke geval. Die implementering van gekrulde vinne is dus 'n opsie by lae vloeitempo's, waar die drukval nie drasties verhoog sal word nie.

Daar is bevind dat die warmte-oordragskoëffisiëntverhoging met 'n vloeitempo van minder as 0,035 kg/s, groter sal wees as die drukvalverhoging. By die ontwerppunt, wat 0.0326 kg/s is, verhoog die warmte-oordragskoëffisiënt met 23 % gepaard met 'n toename in drukval van 20 %. Die vervaardiging van hierdie komplekse vinne is egter baie duur, wat die implementering van gekrulde vinne uitdagend maak.

Acknowledgements

I would like to express my sincere gratitude to the following people and organisations:

- My Lord and saviour Jesus Christ through whom all things are possible.
- Prof TW von Backström and Dr M Lubkoll for their continuous guidance and support throughout the project.
- My parents who supported me and kept me motivated at tough times.
- My colleagues and friends - thank you for making it an enriching experience and a great learning curve in my life. Thank you for lending a helping hand when needed.

Contents

List of Figures

List of Tables

Nomenclature

Variables

d	Diameter	[m]
D_h	Hydraulic diameter	[m]
D_c	Coil diameter	[m]
f	Darcy friction factor	[−]
k	Thermal conductivity	[W/m·K]
L	Length	[m]
L_t	Tube length	[m]
$\dot{m}$	Mass flow rate	[kg/s]
Nu	Nusselt number	[−]
p	Pressure	[Pa]
Δp	Differential pressure	[Pa]
R	Coil radius	[m]
Re	Reynolds number	[−]
Re_{D}	Reynolds number (diameter)	[−]
Re_{crit}	Critical Reynolds number	[−]
V	Velocity	[m/s]
h	Heat transfer coefficient	[W/m^2·K]

Greek symbols

ρ	Density	$[\mathrm{kg/m^3}]$
η	Efficiency	$[-]$
η_w	Efficiency at the wall	$[-]$
ζ	Darsy fritcion factor	$[-]$
δ	Dimensionless curvature	$[-]$
λ	Dimensionless torsion	$[-]$
ε	Dissipation of turbulence energy	$[-]$
ω_k	Angular velocity	$[\mathrm{rad/s}]$
k	Turbulence kinetic energy	$[-]$

Abbreviations

CFD Computational fluid dynamics
CSP Concentrating solar power
HT High temperature
IT Intermediate temperature
LT Low temperature
ORC Organic Rankine cycle
PV Photovoltaic
RANS Reynolds-average-Navier-Stokes
SCRAP Spiky central receiver air pre-heater
SUNSPOT Stellenbosch University solar power thermodynamic cycle
TKE Turbulence kinetic energy

Chapter 1

Introduction

A system such as a concentrating solar power (CSP) plant is one of the ways to harness solar energy. This rapidly evolving technology contributes to the renewable and sustainable energy agenda of the world. An example of a possible next generation thermodynamic cycle for application in CSP is the SUNSPOT, which represents the Stellenbosch University Solar Power Thermodynamic cycle. It is one of the CPS technologies currently being investigated by Stellenbosch University. This specific system, shown in Figure 1.1, differs from other systems by using air instead of oil or molten salt as working fluid. The other defining characteristic is that it is a combined cycle with a rock bed storage.

Due to air being used as the heat transfer fluid, new air receiver technologies have to be investigated to heat the air in the gas turbine. This is why the

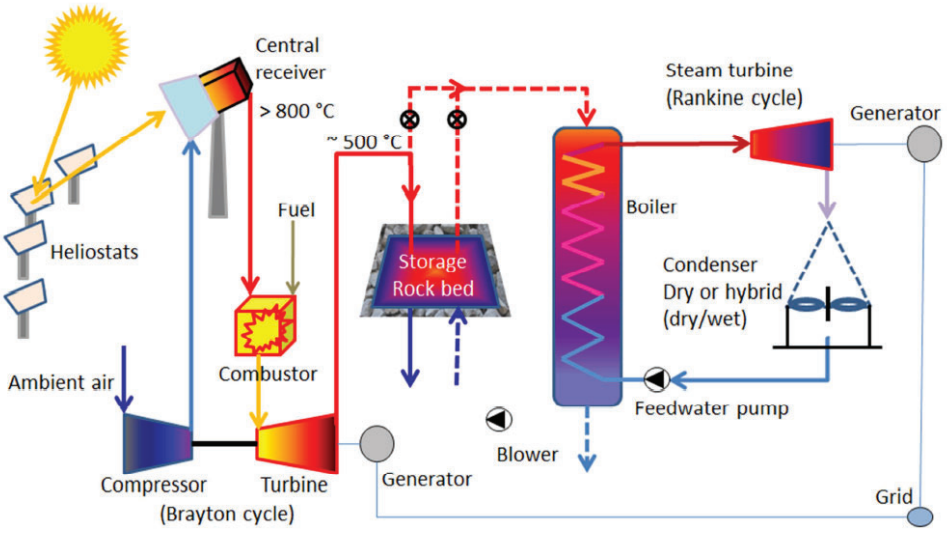

Figure 1.1: SUNSPOT cycle (Kröger, 2012)

SCRAP (Spiky Central Receiver Air Pre-heater) receiver concept was introduced. A study done by Lubkoll *et al.* (2017) indicates the potential of the design of the spikes in the receiver. It is clearly stated that there is much room for improvement.

1.1 Motivation

The main goal of a CSP receiver is to effectively absorb solar radiation concentrated onto the plant's receiver whilst keeping losses, which include radiation losses, reflection losses and convective losses, to a minimum. With the SCRAP receiver concept the radiation loses are minimised due the view factors of each spike being very small. The tip of a spike has a large view factor, but it is internally impinged with cool air, making the heat transfer coefficient large (compared to pipe flow).

The receiver can be improved by enhancing the heat transfer characteristics of the spikes. By improving the rate at which the heat transfer fluid (air) absorbs heat from the metal spikes, the possibility for heat to be lost to the surroundings can be reduced. Taking this into account it shows that improving the spikes are of vital importance.

1.2 Objectives

The main objective of the project is to successfully modify, design and test a SCRAP spike section with helically swirled fins to improve the heat transfer characteristics/efficiency. The objectives are the following:

1. How much does a swirl in the SCRAP increase the heat transfer coefficient?
2. How much does a swirl in the SCRAP increase the pressure drop?
3. Demonstrate that CFD can be used to reliably model the flow and heat-transfer characteristics of a spike with helically swirled fins for design or analysis purposes.

Chapter 2

Literature Review

2.1 Solar energy

Solar energy has the most potential of all the renewable resource (Paper *et al.*, 2003). Within 5.7 hours the earth is irradiated with more energy than could be consumed by the entire global population in a year. If only a fraction of the solar energy could be harnessed and distributed when required, it could supply the world's energy demand in a sustainable and clean manner.

The two most common solar technologies for power generation are Photo-Voltaic (PV) and CSP systems. A disadvantage of solar power generation is that is can only harness irradiation during the day whilst peak power consumption in South Africa occurs during the evenings. PV plants typically have feasibility problems with storage seeing that solar energy is directly converted into electricity. Battery systems are in place to store the electricity, but they increase the cost exponentially and are limited when it comes to storage size (Weniger *et al.*, 2014). CSP plants, contrary to PV plants convert concentrated light into thermal energy which is more economical to store (Duffie *et al.*, 2003).

2.2 Typical CSP cycles

In the following section two thermodynamic cycle configurations namely high-efficiency single cycles and combined cycles will be introduced.

2.2.1 High-efficiency single cycles

The Rankine and Brayton cycles are the basis of high-efficiency cycles and represent thermal power plants in the simplest configuration. A basic Rankine cycle incorporates four stages. The first stage is the compression of a liquid working fluid to achieve high pressures. The second stage is the heating and

vaporization, of the working fluid, by the heat source, followed by its expansion through a turbine to lower pressures and the generation of mechanical work. The last stage is the cooling stage to change the working fluid back to its initial state. Brayton cycles consist of similar processes with the main difference being that the working fluid stays in a single phase throughout the entire cycle.

Solar facilities such as Khi Solar One (a solar tower CSP plant located in the Northern Cape Province of South Africa), even when implementing recovery systems like regenerators or feedwater heaters have a maximum efficiency in the range of 37 %-42 % for the steam plant (Mancini *et al.*, 2011). CSP parabolic trough systems using sub-critical steam Rankine cycles have been limited at the turbine inlet temperature to temperature of less than 400 °C. This is due to the low flux and the limitation of the heat transfer fluid namely oil (Dunham and Iverson, 2014). Systems directly generating steam or using molten salt as working fluid in current state of the art parabolic trough systems can increase the turbine inlet temperature to 565 °C (Price *et al.*, 2002).

A conceptual design of a 100 MW_e molten salt power tower plant have temperature and pressure limitations at the receiver outlet of 565 °C - 600 °C. Steam is superheated to approximately 540 °C at 130 bar and reheated to a temperature of 538 °C at 28 bar (Pacheco *et al.*, 2011). Further operating temperatures are shown in Table 2.1. This cycle with wet cooling typically has an overall thermal efficiency of 42 %.

Table 2.1: Operating specifications

Fluid	Temperature (°C)	Pressure (bar)	Mass flow rate (kg/s)
Hot salt	560	12.0	665
Cold salt	288	2.3	665
Feedwater	234	140	98
Superheated steam	540	132	97
Reheat steam	538	28	85

Advanced high-power multiple-reheat helium Brayton cycles operating at turbine inlet temperature of 750-850°C are predicted to have efficiencies of up to 50% (Forsberg *et al.*, 2007). These high temperatures are achievable in current CSP technologies and are remarkably higher than the operating temperatures in subcritical steam Rankine cycles. The Brayton cycle using supercritical carbon dioxide as working fluid also shows potentially higher efficiencies (Iverson *et al.*, 2013).

Research done by Dostal *et al.* (2006) showed a thermal efficiency of 49.25 % with a turbine inlet temperature of 880 °C for a helium Brayton cycle and 46.07 % with a turbine inlet temperature of 550 °C for a supercritical CO_2 Brayton cycle. Even though supercritical carbon dioxide has a lower efficiency, it has a much lower volumetric flow rate than helium (by a multiple of approximately 5) which leads to smaller turbomachinery requirements.

2.2.2 Combined cycles

Combined cycles consist of multiple thermodynamic cycles. These cycles have one primary high temperature cycle called the topping cycle, and one or more low/lower temperature cycles called the bottoming cycles. Even though advancements have been made in supercritical carbon dioxide and helium single cycles, it is speculated that combined cycles are needed to operate at higher efficiencies (Dunham and Lipiński, 2013).

It has been shown that combined cycles, despite having an increase in capital cost, are more economically effective than single cycles due to the thermal efficiency increase (Klimas and Becker, 1991). A topping Brayton cycle permits the optimum use of the concentrated solar energy provided to the CSP plant where the operating temperatures are much higher than that of subcritical Rankine cycles (McGovern and Smith, 2012).

An example of a combined cycle is one that comprises of a topping Brayton cycle and a bottoming Rankine cycle (RC) for waste heat recovery (Chacartegui *et al.*, 2009). A study done on alternative organic Rankine cycles as bottoming cycles in combined cycle power plants showed that with a turbine inlet temperature of 1500 K (1226.85 °C) can have an efficiency of up to 53.91,% (Chacartegui *et al.*, 2009). A comparison done by Chen *et al.* (2010) on a variety of working fluids for the conversion of low grade heat in a bottoming cycle showed that dry and isentropic fluids are preferred in RC. The study also showed that superheating dry fluids could affect the cycle efficiency negatively, while it is necessary for wet fluids to function in an RC. Additional heating sections can thus be reduced when using dry fluids. Consequently, fluids possessing low critical temperatures and pressures could potentially be implemented in the supercritical Rankine cycle. A schematic of a typical combined cycle is shown in Figure 2.1.

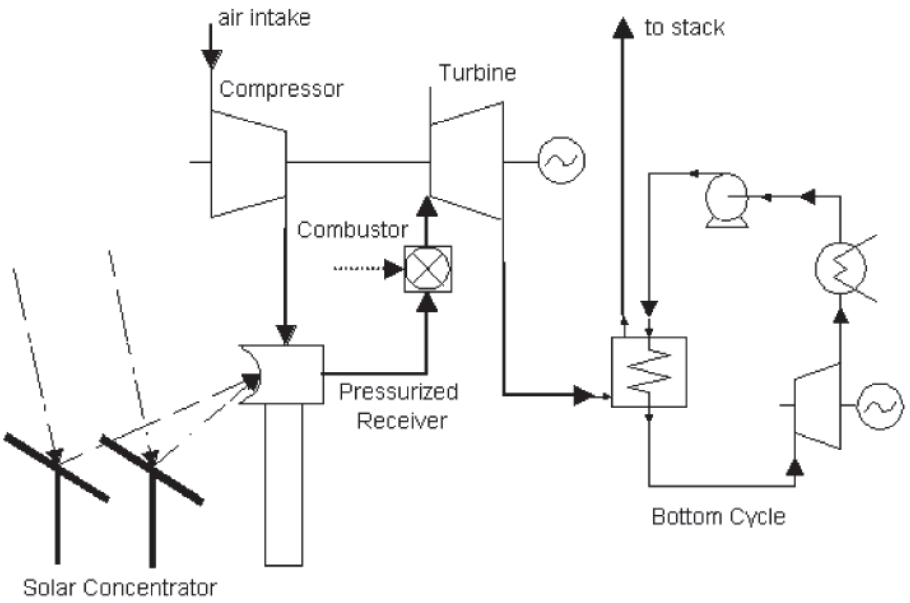

Figure 2.1: Combined cycle with a topping Brayton cycle and bottoming Rankine cycle (Schwarzbözl *et al.*, 2006)

Characteristics of heat transfer fluids

A study done by (Becker, 1980) compared potential heat transfer fluids for CSP usage by their transport and thermal properties. He focused on a wide variety of fluids including hydrogen, air, water vapour, helium, ammonia, thermal oil, potassium, sodium and mercury. The important thermal properties of heat transfer fluids and reason for importance are shown in Table 2.2

Table 2.2: Heat transfer fluid characteristics

Characteristic	Reason
Low lower temperature limitation	Low solidification temperature
High upper limitation	Thermal stability (evaporation temperature)
Low viscosity	Decrease pumping requirements
High thermal conductivity	Heat transfer fluid and receiver temperature close to equal
Possibility of being working fluid	Decrease complexity of system
Chemical compatibility with contact materials	Increase lifespan and decrease corrosion
High availability and low cost	Economical
Low environmental hazard (flammability, toxicity, explosivity)	Safety

2.2.3 Types of heat transfer fluid

Oils

Most parabolic trough systems use oil as working fluid (NREL (2013a)). The operating temperature of these oils are limited to approximately 400 °C (Dow Chemical Company (2001)). These low temperatures limit the thermal efficiency of the system. Other disadvantages of oil include excessive costs, flammability and the degradation over time.

Molten salts

A CSP plant that used molten salt as heat transfer fluid, including a molten salt storage system is parabolic trough concentrators (Andasol-1) (Dunn *et al.*, 2012). The operating temperature of the so called Solar Salt ranged from 290 °C - 565 °C with a mass fraction combination of 40 % KNO_3 and 60 % $NaNO_3$.

Although the solar salt can reach temperatures of up to 600 °C without becoming unstable the upper limit of was chosen to minimise the corrosion rate for the stainless-steel piping (Pacheco and Dunkin, 1996). The lower limit temperature in place to provide a safety region to prevent solidification of the salt which occurs at approximately 221 °C.

The heat transfer characteristics of molten salt is average (Santana, 2013). The reason behind this statement is due to the high density and an average specific heat capacity which leads to a low flow rate. Elevated temperatures arise on the outside of the receiver tubes due to the low flow rates causing large radiation losses.

There are two ways to improve the heat transfer between the receiver tube and heat transfer fluid. The simplest way is by increasing the flow rate and inducing turbulence or by using spiral tubes (Yang *et al.*, 2010). Another method is by improving the receiver's optical efficiency by using pyramid-like spikes which traps the light and radiation as demonstrated by Garbrecht and Kneer (2012).

Liquid metal

Alternative heat transfer fluids do not have the limiting upper and lower operating temperatures that molten salt has. Some liquid metals have boiling temperature of up to 1600°C and freezing (solidification) temperatures well below zero. This nearly eliminates the possibility of solidification within the receiver, pipes or valves. Another advantage is that low pressure operation is possible at the high temperatures required for Brayton or next generation Rankine cycles. The low-pressure operation allows for the use of thinner pipe/wall thickness of the receivers leading to higher thermal efficiencies and reduced thermal strain caused by thermal expansion (Boerema *et al.*, 2012; Lata, 2018).

Liquid metals also have outstanding heat transfer characteristics accompanied with low viscosity. The temperature gradient of the flow, due to the high thermal conductivity of liquid metal will be particularly small within the pipe. The properties of these heat transfer fluids will eventually allow for higher fluxes on the receiver as well as higher thermal efficiencies.

Liquid metals show potential as heat transfer fluid allowing for very high operation temperatures at low pressure, resulting in higher efficiencies and low pressure drops. However, the disadvantages include difficulties with maintenance, operation, safety, steel corrosion, high cost and not being able to be used as a direct storage medium.

Air

When considering a Brayton cycle air poses great potential as heat transfer fluid. It is non-hazardous, freely available, does not require a heat exchanger for co-firing and is basically free of cost when compared to the cost of other heat transfer fluids. The downside of using air is that it has very low densities and heat transfer characteristics, demanding the use of large heat exchangers and receivers. As a result, pressurisation is needed for the application of air in a CSP receiver. The performance of a gas turbine is dependent on the pressure

drop between the compressor and expander. Bearing this in mind, attention needs to be paid to the pressure drop in this high-pressure cycle.

In the Solar hybrid gas turbine electric power system (SOLGATE) project a 250 kW_e central receiver CSP prototype was developed and tested by the Directorate-General for Research and Innovation (European Commission, 2005). The system consists of three air-cooled receivers connected in series, a high temperature (HT), an intermediate temperature (IT) and a low temperature (LT) receiver. Pressurised air is heated from 300 °C to 550 °C in the LT receiver, then from 550 °C to 730 °C in the IT receiver and lastly heated to 960 °C in the HT receiver. A gas combuster raises the temperature to 1200 °C. In using the gas combustor, the efficiency of the gas turbine is enhanced.

Later the Solar-Hybrid Power and Cogeneration (SOLHYCO) project was launched, succeeding the SOLGATE project. It consisted of a 100 kW_e microturbine with a recuperator and bio-diesel combustor (DLR, 2010). The recuperator increases the inlet temperature of the receiver considerably, enabling the use of a single HT receiver instead of three. The receiver design was changed from a pressurised volumetric receiver to a pressurised tubular receiver implementing novel profiled multilayer tubes. These tubes were not installed due to manufacturing delay, however, expected homogenization of the tube temperatures were shown by laboratory testing. A maximum temperature of 800 °C was reached for the receiver outlet. Design shortcomings that limited the outlet temperature and receiver efficiency were identified and solutions were proposed.

Summary for air:
Much research has been done on air as heat transfer fluid. This is due to several factors including the availability of air and the vast experience with it as working fluid and as a heat transfer fluid. The high operating temperature promotes a high thermal efficiency and enables the implementation of a combined cycle, however, the low thermal conductivity and low density poses some difficulties with the heat transfer.

2.3 Stellenbosch UNiversity Solar POwer Thermodynamic cycle

2.3.1 SUNSPOT

The SUNSPOT cycle is one of the solar thermodynamic cycles currently being investigated by Stellenbosch University. The cycle consists of a topping Bryton cycle and a bottoming Rankine cycle. The topping Brayton cycle uses air

as working fluid and the bottoming Rankine cycle uses steam.

The schematic of the SUNSPOT cycle is shown in Figure 1.1. Solar irradiation is concentrated by means of heliostats onto the central receiver. Ambient air is compressed and then heated by the receiver to temperatures above 800 °C (Kröger, 2012). This hot air is then ducted to the turbine which generates electricity to the power grid as well as driving the compressor. Air leaves the turbine at approximately 500 °C from where it is ducted to a thermal rock bed storage (Kröger, 2012).

During downtimes or night times air is pumped from the thermal rock bed storage across a finned tube boiler. Steam is generated by the boiler which drives the secondary turbine (Rankine cycle) to supply the electricity demand at night. The steam is then cooled in a condenser which rejects heat to the environment.

With the implementation of biofuel or gas burners or combustors upstream of the turbine in the topping cycle the fluctuation in electrical output due to the constant change in solar irradiation can be eliminated. With this addition the turbine temperature and efficiency will consequently maximise the plant's power output.

2.3.2 Receiver efficiency

There are three types of losses in a receiver system namely: pumping losses, thermal losses, and optical losses.

Pumping losses

Pumping losses occur within the system cycle due to head loss and fluid flow friction. These losses are of secondary concern seeing that they contribute to less than 2 % of the total losses in a CSP plant system (Pitz-paal *et al.*, 2015).

Thermal losses

The thermal losses consist of radiation, conduction and convection losses. Radiative losses on a receiver are a result of the high temperature of the receiver radiating heat to the environment. Convective losses are losses from the receiver's exposed area to ambient air. Conduction losses occur from the receiver to the tower. The conductive losses are minor losses and are typically neglectable.

The size of these losses differ from receiver to receiver seeing that it is influenced by the area exposed to natural conditions and ambient air as well as the receiver's emissivity and absorptivity. The convection losses are directly

proportional to the difference in receiver surface temperature and the ambient air temperature. The radiative heat losses are directly proportional to the difference between the receiver surface absolute temperature (in Kelvin) to the power four and the ambient air temperature to the power four.

Optical losses

The optical losses on a receiver involves reflection and spillage losses. To achieve high emissivity/absorption, in the case of the spike, a low reflectivity is ideal. This can be achieved by applying selective coatings to ensure maximum absorption (Stine and Geyer, 2001). Spillage losses is a result of sun rays reflected from the heliostats missing the receiver.

Optical field losses include shadowing and blocking, the cosine effect, and mirror reflectance losses. Shadowing losses happens when a heliostat is in the shade of another heliostat, while blocking is when the reflected sun rays are blocked from the receiver by another heliostat. The cosine effect is a major factor when determining the optical losses. The heliostats are positioned by a tracking system so that the surface normal divides the angle between the receiver and the sun's position. The effective reflection area of the heliostat is reduced by the cosine of half this angle. Mirror reflectance is due to the mirror absorbing some of the radiation instead of reflecting it. Age and dust are the cause of this loss and it can be up to 10 % (Stine and Geyer, 2001). To minimise these losses advanced tracking systems and the optimal field design layout are employed.

2.3.3 Spiky Central Receiver Air Pre-Heater (SCRAP)

Up to date not many pressurized air receivers have been considered. The SCRAP concept receiver is thought to be able to heat up air to above 800 °C while other pressurized receivers can reach temperatures higher than 1000 °C. Even though systems like the SCRAP cannot reach these elevated temperature, the system is believed to be more robust, cheaper and less complex.

The SCRAP receiver is an external metallic tubular receiver with a multitude spikes protruding from the receiver centre. It consists of multiple spikes absorbers assembled in a half spherical form. An example of the concept is presented in Figure 2.2.

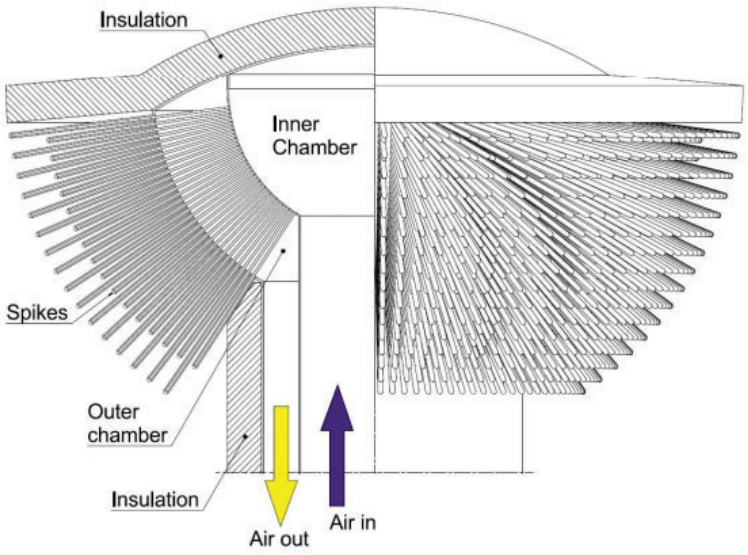

Figure 2.2: SCRAP receiver with cross-section (Kröger, 2008)

Each spike consists of two tubes, the inner tube which serves as the cold air supply to the spike tip, and the outer tube which transports air back to the centre of the receiver. Cold air enters in the centre of the receiver, from there the air enters the spikes. The cold air travels through the inner tube towards the tip of the spike. The cold air impinges the spike tip at which stage it is redirected back 180° and travels along the outer tube. Concentrated rays heat up the tip and outer area of the spike, heat is then transferred through the spike to the air. The air flow is shown in Figure 2.3 (Figure B4 in Appendix B contains more detail)

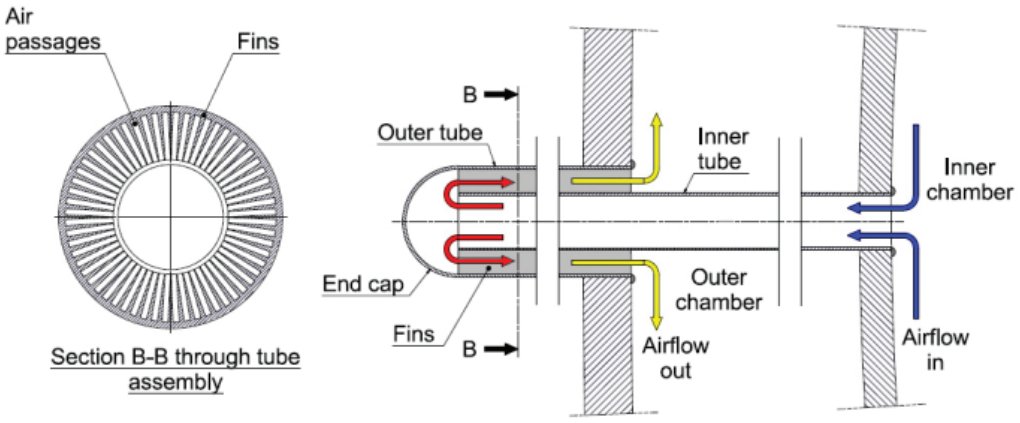

Figure 2.3: Straight tube geometry (Kröger, 2008)

The SCRAP receiver can be classified as a external macro-volumetric tubular pressurised receiver (Lubkoll, 2017). The spikes emulate a porous like surface, permitting concentrated radiation to penetrate the spike material. Further, it is known that the most exposed section is the spike tip which experiences the highest cooling effect caused by the impingement of the cold air.

The air is further heated as it flows from the tip, through the internally finned tube section, towards the receiver's centre or outer chamber. The volumetric effect is improved by having the highest air and absorber temperatures at the spike outlet, discharging into the outer chamber of the receiver.

Further, it is predicted that the highest pipe surface temperature will be at the area of lowest radiation, permitting the utilisation of high fluxes without causing the absorber pipe to overheat. The SCRAP receiver concept is also one of the only concepts (for a pressurised air receiver) that operates without a quartz glass window.

The modification of current straight fins implemented within the tube section of the spikes is to be investigated. This will be done to achieve higher heat transfer coefficients while maintaining a marginal pressure drop increase.

2.4 Expected benefits of helically swirled fins

A possible way to improve the heat transfer efficiency of the spikes is to have the fins located on the inside of each spike helically swirled. In this project, the possible application of these helically swirled fins will be investigated.

Helically coiled ducts are widely used in industries such as industrial heat exchangers, process plants, heat recovery systems, and the food industry. They are known for their compact size and heat transfer performance. They are preferred because of their low energy consumption as well as low maintenance cost (Ghobadi and Muzychka, 2016).

The heat transfer rate is much higher in helical channels (Xing *et al.*, 2014). This is because of the presence of a dimensionless tortuosity (λ), defined in equation 2.3, which has large effects on the flow field. It was found that the heat transfer coefficient can be increased by reducing the diameter ratio, the coil diameter versus the tube diameter, in the study of helical coiled tubes by Ali (2004). In Wu *et al.* (2009) the study of turbulent flow and heat transfer in a helical coiled tube, concluded that the helical effect is smaller in turbulent flow than in laminar. This causes a decrease in wall friction and heat transfer coefficient in laminar flow. Further, it is known that the increase in heat transfer is large for tubes with greater curvature ratio, as defined by Xing *et al.* (2014).

Keeping all of these factors in mind it is necessary to note that not much research has been done on helically coiled/swirled rectangular ducts in regard to heat transfer. Mori *et al.* (1970) conducted a study on forced convective heat transfer in a curved channel with a square cross section but with only half a turn which does not show the same helical effect as multiple turns would.

A study done by Xing *et al.* (2014) on convective heat transfer characteristics in helical rectangular ducts provides further knowledge on parameters effecting the helical effect in a duct. The geometry as described by Xing *et al.* (2014) is indicated in Figure 2.4.

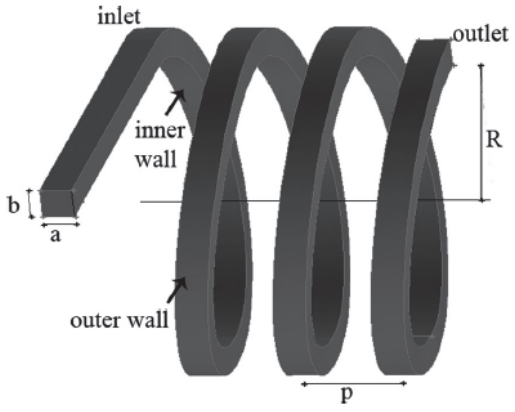

Figure 2.4: Rectangular coil geometry (Xing *et al.*, 2014)

Where b is the height, a the width, R the curvature radius of the coils and p the pitch of the duct. From this geometry the hydraulic diameter can be derived using equation 2.1, where A is the cross-sectional area of the flow ($b \times a$) and P is the wetted perimeter of the flow ($2b \times 2a$). Other important parameters as described by Xing *et al.* (2014) are the dimensionless curvature (δ) and tortuosity (λ) shown in equations 2.2 and 2.3:

$$D_h = \frac{4A}{P} \tag{2.1}$$

$$\delta = \frac{a}{R} \tag{2.2}$$

$$\lambda = \frac{p}{2\pi R} \tag{2.3}$$

Effect of the pitch:
When the dimensionless curvature and Reynolds number are given, the heat transfer coefficient at the inner and outer wall are similar with minor differences. A large pitch promotes flow resistance to a minor extent, causing the heat transfer properties to have slight dependency on the pitch.

Effect of the curvature:
According to Xin and Ebadian (1997) in the study of the effects of Prandtl numbers on local and average convective heat transfer characteristics in helical pipes the Nusselt number increases when the curvature ratio is increased from 0.0267 to 0.0884 in helical pipes while subjected to laminar flow. Wu *et al.* (2009) on the other hand found that higher curvatures result in a decrease of the average Nusselt number for turbulent flow in helical coil tube possessing a curvature ratio from 0.1 to 0.3. These experimental differences could be due to the existence of a critical curvature ratio. The average Nusselt number is higher when the curvature ratio is increased causing the turbulent disturbance to have stronger effect. In the other case, in the presence of turbulent flow, the centrifugal force causes secondary flow to have a strong effect in helically coiled tubes. Xing *et al.* (2014) found that the heat transfer rate on the inner wall is mostly affected by varying the curvature ratio, and that a lower curvature ratio reduces the friction factor.

Effect of parameters of cross-sectional area:
The heat transfer coefficient of a duct can be enhanced by increasing the height to width ratio (Xing *et al.*, 2014). That said, decreasing the height to width ratio can decrease the heat transfer coefficient noticeably. Large height to width ratios have much lower flow resistance thus decreasing the pressure loss in the duct.

Curvatures in ducts make fluids behave vastly differently when it comes to flow patterns. This is because of vortex structures that are produced promoting fluid mixture and thus forced convection (Soong and Yan, 1999). Centrifugal effects in the axial fluid motion is caused by flow in curved ducts, which does not manifest in straight ducts.

Two main effects manifest in the flow of curved ducts. The first one is that the curvature generates a positive radial pressure gradient, acting from the inner to outer wall, in the fluid's cross-sectional area. The other is that it generates lateral fluid movement that over lapses the axial flow. The fluid movement causes the axial flow to make a spiral movement through the duct, this is also known as secondary flow. A positive pressure field, which is a radial pressure gradient acting from the inner to the outer duct wall, and the viscous effect both work against the secondary fluid movement damping its effect. This causes a stagnant fluid region close to the outer wall (Dean, 1928).

In the stagnant region near the outer wall a localized fluid circulation is stimulated by the pressure gradient at high axial flow rates which creates additional sets of rotating vortices (secondary flow).

When high Reynolds numbers are achieved in a curved duct, secondary flows are created by the centrifugal forces. The secondary flows form pairs of counter rotating vortices. These stream wise orientated vortices are called Dean vortices and cause the phenomenon known as Dean's instability (Ligrani, 1994).

Two separate criteria are identified to determine the onset of the Dean vortices (secondary flow) in rectangular ducts. The first technique is based on the wall pressure gradient while the other utilizes the dimensionless helicity. Both techniques were developed by Chandratilleke and Nadim (2014) and validated to have a high consistency and reliability in predicting critical flow conditions of Dean's instability.

2.5 CFD theory

In this section the standard k-ε, realizable k-ε, RNG k-ε, standard k-ε and SST k-ω along with their advantages and disadvantages will be discussed (Wasserman, 2016).

The k-ε method is well known and widely used. The reason for this is due to its limitations being well known (Wasserman, 2016). The limitations include adverse pressure gradients, jet flows and some difficulty solving epsilon.

The most widely used is the realizable k-ε model (Sofu *et al.*, 2004). The model represents the most proven, well quantified and widely-documented of all closures. The model has improved performance for planar surfaces, round jets, rotation, recirculation and streamline curvature. It also improves the boundary layer under strong adverse pressure gradients or separation (Sofu *et al.*, 2004).

The RNG k-ε on the other hand can underestimate the k value and produce lower turbulence levels causing a less viscous flow. This creates more realistic flow features when dealing with complex geometries. However, it is stated that RNG k-ε offers little or no advantage over the realizable k-epsilon model(Popoola and Cao, 2016).

The most significant advantage of the k-ω model is that it may be applied throughout the boundary layer without further modification (Wasserman, 2016). It is generally applied to turbomachinery simulations where strong vortices are present. The k-ω over-predicts separation and can over-predict shear stresses of adverse pressure gradient boundary layers (Wasserman, 2016). Furthermore, the model has issues with free stream flows and is also very sensitive to inlet boundary conditions, which is not the case for the k-ε model.

The limitations of k-ω include difficulty of convergence compared to k-epsilon and sensitivity to initial conditions (Wasserman, 2016). Furthermore, the standard k-ω model can be used in this mode without requiring the computation of wall distance. It over-predicts separation, but performs well in the near wall region and for swirling flows.

The SST k-omega model is an enhancement of the original k-omega model (Wasserman, 2016). It addresses some specific flaws of the base model, such as the sensitivity to freestream turbulence levels and an improved ability to predict separation and reattachment. It also requires limiters to improve the prediction of stagnant regions of the flow. Additionally, it has issues predicting turbulence levels and complex internal flows and it doesn't take buoyancy into account. The performance of SST k-ω is not very different from the realizable k-ε two-layer model (Wasserman, 2016).

In conclusion the realizable k-ε is suitable for modelling a helical duct. It performs well in rotations and streamline curvatures and also improves the boundary layer under strong adverse pressure gradients as previously stated. Furthermore, it is a well-known model and other models do not hold major advantages to it.

2.6 Empirical correlations

In this section empirical correlations are used to provide motivation for a numerical simulation and experimental testing. These results will provide the insight on the secondary flow that occurs within the tube and the effects it has on the heat transfer rate.

There are several papers published on the empirical heat transfer in a pipe for turbulent flow. However, many of these semi-empirical correlation obtained experimentally contain significant errors which are troublesome to estimate (Petukhov, 1970). Some accurate experimental data have been reported. These heat transfer correlations were mainly measured for air and water, being accurate for a range of $0.7 \leq Pr \leq 10$. For the case being investigated this range is acceptable. The Reynolds number being investigated range from $1500 < Re < 55\ 000$ and methods for predicting the heat transfer coefficients and friction factors follow.

2.6.1 Straight duct

Theoretically predicted results are subsequent to many factors. One of the most important factors is the method of heat applied to the system which plays a vital role in choosing the correct correlations. The relation of the Nusselt number to Reynolds number is different for the heat sources with constant flux and constant temperature (Petukhov, 1970). This difference usually only occurs with low Prandtl numbers (liquid metal). The difference is also much smaller at high Reynolds and Prandtl numbers. It is said that for $Pr \geq 0.7$ and $Re \geq 10^4$ both the constant heat flux and constant temperature heat source stay within 10 % from each other making correlations valid for any heat source (Petukhov, 1970; Kakac *et al.*, 1987).

For comparison, calculations on a straight duct had to be done first. The friction factors and Nusselt numbers are calculated using Petukhov's equation for friction factor (Basse, 2017) and Dittus and Boelter for the Nusselt number (Cengel, Yunus A. Ghajar, 2015):

$$f_s = (0.790 \ln Re - 1.64)^{-2} \tag{2.4}$$

and

$$Nu_s = 0.023 Re^{0.8} Pr^{0.4} \tag{2.5}$$

2.6.2 VDI

The geometry of a coil, according to the VDI heat atlas, is given by Figure 2.5.

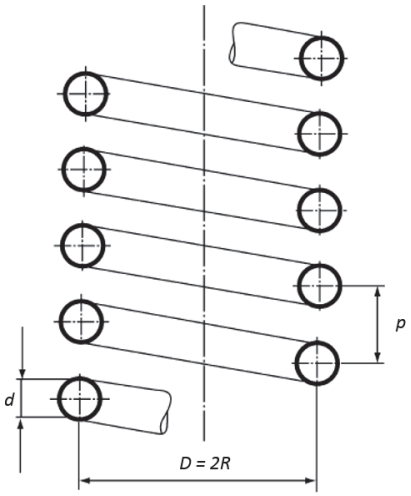

Figure 2.5: Coil Geometry (Stephan *et al.*, 2010)

Using the hydraulic diameter, shown in equation 2.1, the VDI equations can be applied to a rectangular duct (Stephan *et al.*, 2010). It is stated that Nu stays within a 15 % error when using the following equations:

$$Nu = 3.66 + 0.08\left[1 + 0.8\left(\frac{D_h}{D}\right)^{0.9}\right] Re^m Pr^{\frac{1}{3}} \left(\frac{Pr}{Pr_w}\right)^{0.14} \tag{2.6}$$

valid for laminar flow $Re \leq Re_{crit}$ where

$$m = 0.5 + 0.2903\left(\frac{D_h}{D}\right)^{0.194} \tag{2.7}$$

and

$$Re_{crit} = 2300\left[1 + 8.6\left(\frac{D_h}{D}\right)^{0.45}\right] \tag{2.8}$$

and

Pr/Pr_w attempts to explicitly account for the fact that the viscosity of the fluid next to the wall is different from that in the bulk at any axial location.

For turbulent flow the following equations are applied ($Re > 2.2 \times 10^4$):

$$Nu = \frac{\left(\frac{\zeta}{8}\right) RePr}{1 + 12.7\sqrt{\frac{\zeta}{8}}\left(Pr^{\frac{2}{3}} - 1\right)} \left(\frac{Pr}{Pr_w}\right)^{0.14} \tag{2.9}$$

where

$$\zeta = \left[\frac{0.3164}{Re^{0.25}} + 0.03\left(\frac{d}{D}\right)^{0.5}\right] \left(\frac{\eta_w}{\eta}\right)^{0.27} \tag{2.10}$$

2.6.3 Kakac

According to Kakac *et al.* (1987) the measured Nusselt number at the outer wall of a helical coil is about 1.5 times that of a straight tube and the inner wall is about 0.5 that of a straight tube. This means that the overall Nusselt number of a helical coil is 20 - 30 % higher than a straight tube. The equation used to calculate Nusselt number for multiple Reynolds numbers are as follow:

$$\left(\frac{Nu_c}{Nu_s}\right) = 1.0 + 3.6\left[1 - \frac{D_h}{D}\right]\left(\frac{D_h}{D}\right)^{0.8} \tag{2.11}$$

is valid for 20 000 < Re < 150 000.

For lower Reynolds numbers, the following equation is used:

$$\left(\frac{Nu_c}{Nu_s}\right) = 1.0 + 3.6\left[\frac{D_h}{D}\right] \tag{2.12}$$

This equation is valid for 1 500 < Re < 20 000 where

$$Nu_s = 0.023 Pr^{0.5} Re^{0.8} \tag{2.13}$$

For the range of 1500 < Re < 8000 the friction factor is calculated using the following equation:

$$\frac{f_c}{f_s} = 0.435 \times 10^{-3} Re^{0.93}\left(\frac{D/2}{a}\right)^{-0.22} \tag{2.14}$$

where f_s is calculated with equation 2.4
Then for Re > 8000

$$f_c\left(\frac{D}{D_h}\right)^{0.5} = 0.084\left[Re\left(\frac{D}{D_h}\right)^{-2}\right]^{0.2} \tag{2.15}$$

These equations are in good correlation with experimental data for air and water and stay within a 10 % variation (Kakac *et al.*, 1987). The friction factor is 1.5 times larger at the outer wall of the coil and 0.5 times smaller at the inner wall of the coil, which is the same as for Nusselt number.

For these equations the wall thermal boundary conditions are not significant for $Pr \geq 0.7$. Therefore, the equations are applicable to the cases where boundaries are insulted and when they are not.

The last two equations used to calculate the Nusselt numbers are the Xin and Ebadian and the Kaya and Teke methods.

2.6.4 Xin and Ebadian

Xin and Ebadian (1997) based their correlation on the average fully developed flow conditions for laminar and turbulent flow (Sleiti, 2011). Five different pipe diameters were used along with several different working fluids when deriving the empirical relationship. The correlations for turbulent flow is shown in equation 2.16

$$Nu = 0.00619 Re^{0.92} Pr^{0.4} \left(1 + 3.455 \left(\frac{D_h}{D}\right)\right) \tag{2.16}$$

where $5 \times 10^3 < Re < 10^5$, $0.7 < Pr < 5$, and $0.0267 < D_h/D < 0.884$.

2.6.5 Kaya and Teke

Kaya and Teke (2005) based their correlation on the fully developed turbulent flow conditions. The Nusselt number calculated by their correlation was determined to be that of the inner wall and is given by equation 2.17.

$$Nu = 0.023 Re^{0.8} Pr^{0.4} \left[1.0572 + 0.1761 \left(\frac{D_h}{D}\right)\right] \tag{2.17}$$

where $0.0266 < D_h/D < 0.1095$ and $15\ 000 < \mathrm{Re} < 135\ 000$

Different thermal boundary conditions were applied for each of the correlations. However, Coronella (2008) has determined that for $Pr > 0.7$ the thermal boundary conditions does not have large effects on the Nusselt number when considering turbulent flow.

Furthermore, each correlation was obtained with a different set of pitches and none of the methods used similar pitches to obtain their correlation. However, as previously stated that the helical pitch of a duct has minimal effects on the Nusselt number, and even more so when considering turbulent flow.

2.6.6 White

White presented one of the first correlations in the turbulent flow range for helical ducts (Guo *et al.*, 2001) and is given as:

$$f_c = 0.31 \left[log \left(\frac{Re}{7}\right)^{-2} + 0.04 \left(\frac{D_h}{D}^{0.5}\right)\right] \tag{2.18}$$

2.6.7 Results

The correlations were employed using a straight and helical duct with the same cross-sectional length and width of 18.04 mm and 3 mm and an inner duct radius of 15 mm. The cross-sectional parameters of the helical duct are

measured perpendicular to the tube and not the direction of flow. The duct geometry is shown in Figure 2.6.

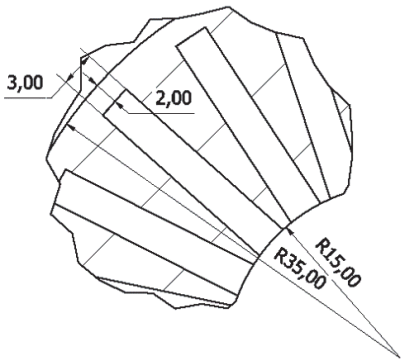

Figure 2.6: Rectangular duct dimensions

With these dimensions the hydraulic diameter is calculated using equation 2.1. The hydraulic diameter for this specific case is thus 5.143 mm and is used for all relevant calculations.

Further results, for Reynolds numbers from $1500 < \mathrm{Re} < 50\,000$, are shown in Figures 2.7 and 2.8. These results are obtained by using the relevant geometrical values of the case being investigated.

Figure 2.7 shows a somewhat linear increase in Nusselt number with an increase in mass flow rate. There are however large differences between the four helical correlations and they must be further investigated by means of a numerical simulation.

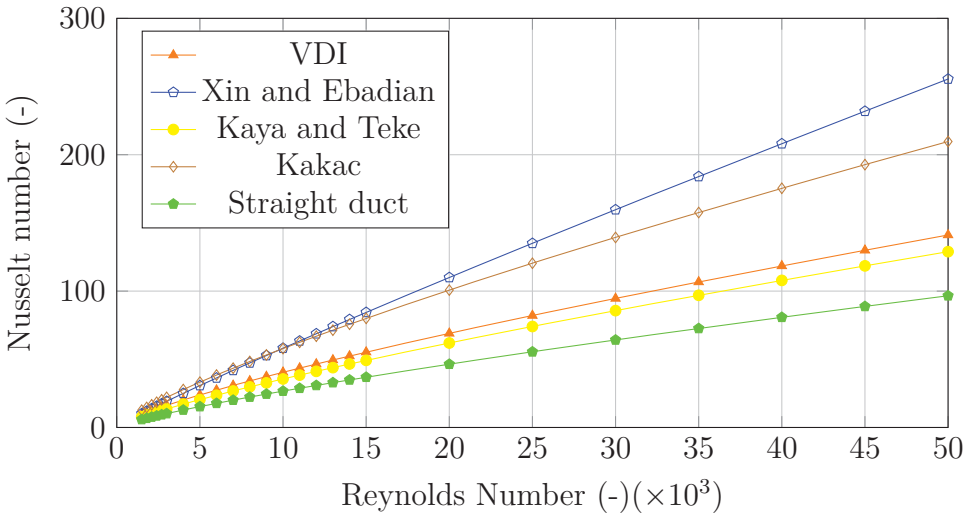

Figure 2.7: Nusselt number over Reynolds number

Even though the results of the various methods used to calculate the Nusselt number for the case stated differ, they all show an improvement over the straight duct. However, the friction factors, shown in Figure 2.8, show an increase in value over the straight duct.

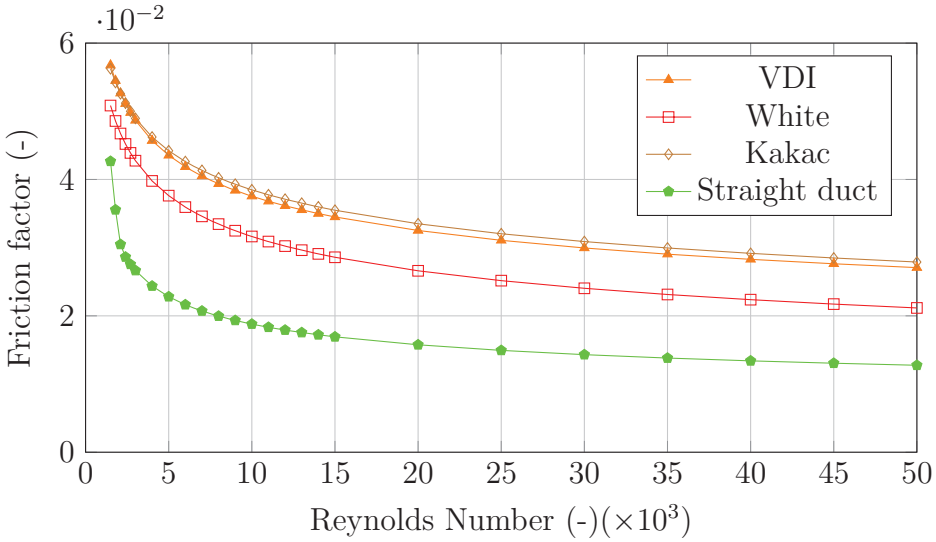

Figure 2.8: Friction factor over Reynolds number

The pressure drop can be calculated using the friction factor obtained in each of the methods and equation 2.19:

$$\Delta p = f\left(\frac{L}{D_h}\right)\frac{\rho V^2}{2} \tag{2.19}$$

where Δp is the pressure drop, L is the length of the duct, D_h is the hydraulic diameter, ρ is the density of the working fluid and V is the velocity.

The pressure drop, visible in Figure 2.9 shows that with the increase in heat transfer capabilities comes the cost of higher pressure drop. The pressure drop at high flow rates is seen to be significantly higher for a curved duct. A way of overcoming this pressure drop is by increasing the discharge head in the system, but this will ultimately decrease the overall efficiency of the system and defeat the purpose of curved ducts.

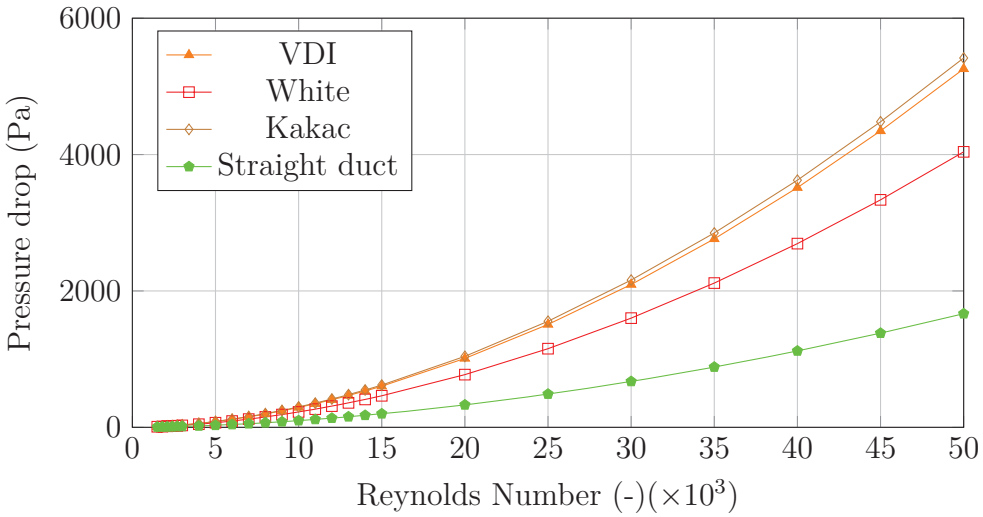

Figure 2.9: Pressure drop over Reynolds number

In Figure 2.10 the heat transfer vs Reynolds number is shown. This is calculated using equation 2.20, accompanied with the relevant characteristics.

$$Nu = \frac{D_h h}{k} \tag{2.20}$$

The trend is the same as for the Nusselt number and looks to be linear of nature.

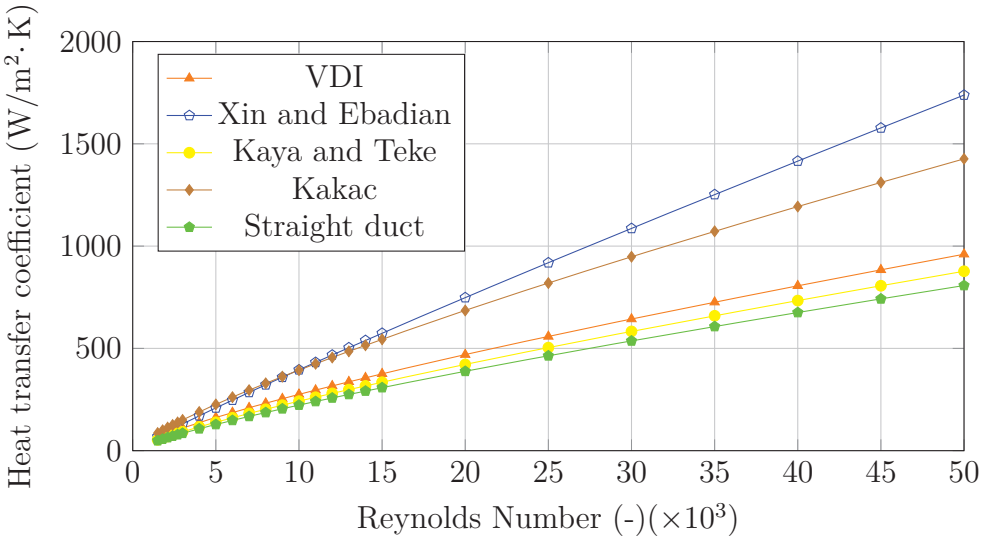

Figure 2.10: Heat transfer coefficient over Reynolds number

Figure 2.11 shows the heat transfer coefficient increase, using the VDI method, with the increased number of rotations within a 200 mm duct section. A small increase in heat transfer coefficient can be seen when the duct rotates 0.1 times over a distance of 200 mm. An increase of 2 % is present with this swirl. Further a duct with two full rotations show a much larger increase of 31 %. This figure shows that 1 full rotation is worth investigating.

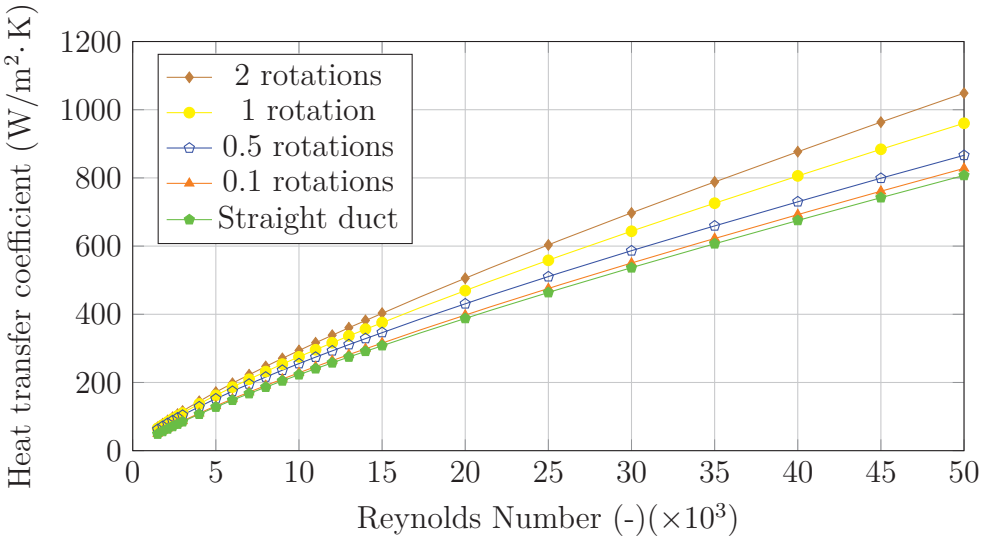

Figure 2.11: Heat transfer coefficient over Reynolds number for different swirl angles

Further analysis on the effect of different swirls on the pressure drop is shown in Figure 2.12. An average increase in pressure drop of 36 % is seen in a duct with 0.1 rotations over a distance of 200 mm. Two full rotations increase the pressure drop with an average of 120 %. The swirls have a larger effect on pressure drop at higher flow rates.

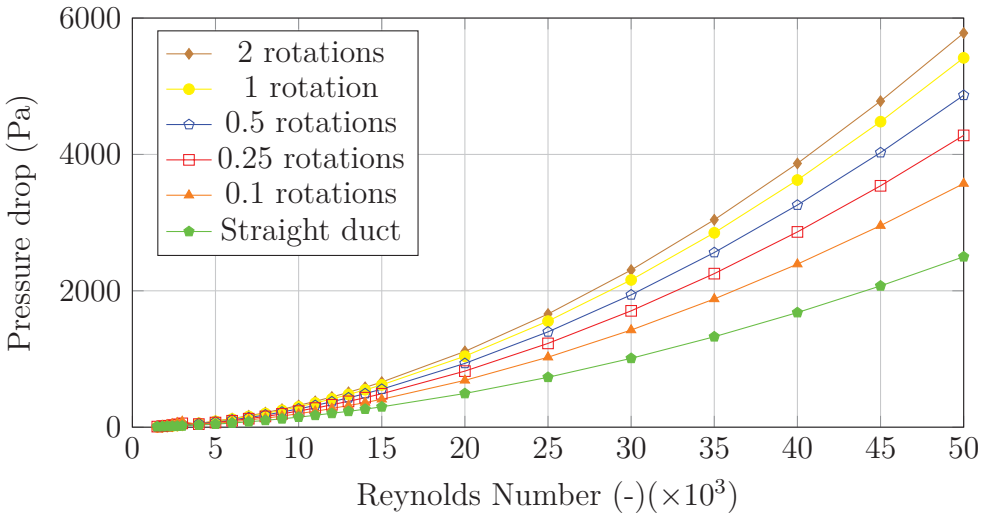

Figure 2.12: Pressure drop over Reynolds number for different swirl angles

Overall the heat transfer is increased linearly whilst the pressure drop increase exponentially. There is an obvious trade-off between the two and a favourable point at which the efficiency will be increased sufficiently while not increasing the pressure drop excessively. For this reason, the calculations provide motivation to further investigate the effect helically swirled ducts could have on the heat transfer capabilities in a SCRAP system.

Chapter 3

Numerical Simulation

The purpose of this chapter is to discuss some background of Ansys Fluent and the formulations used within the program. Furthermore, the numerical simulation will be discussed in detail including the geometry, mesh, grid independence, solution model and results. For simplification of the model only one of the 24 symmetrical ducts will be modelled. The same geometry used in the calculations will be applied to the simulation to have comparable results.

The computational fluid dynamic (CFD) analysis will be compared to the theoretical and experimental results. Accuracy between the CFD and experimental results could motivate further large scale CFD analysis, which refers to the integration of external factors and actual conditions on full SCRAP system.

3.1 Turbulence modelling

Fluid motion is described using Reynolds-average-Navier-Stokes (RANS) equations which is the basis of the turbulence model used in this thesis. This approach is used in several models including the k-ε and k-ω models. The realisable k-ε model is used in this thesis thus, only its formulation will be discussed accompanied with a motivation on why the model was chosen.

Realizable k-ε model

The k-ε realizable method is an improvement on the standard k-ε model (Shih *et al.*, 1995). Three common factors characterise the model. The first is that the model has a variable C_μ, which replaces a constant used in other models. This variable is based on the rotation rates and mean strain. Secondly, the exact transport equation for the mean square of the vorticity fluctuation is used to reformulate a new transport equation for the dissipation rate. Lastly, the model is realisable, meaning the mathematics used are the accurate and satisfies the physics (production term) of turbulent flow causing the Reynolds

stress to always be positive.

Some direct benefits include improved prediction of the spreading rate in planar or round jets as well as providing a superior performance for any flow involving rotation, separation, recirculation and boundary layers under adverse pressure gradients (Shih *et al.*, 1995). Furthermore, this model captures the mean flow of a complex structure, like rotating ducts, well and is thus an appropriate model for this case.

An investigation in the Reynolds stress shows it is possible to write the Reynolds stress as follow:

$$\overline{u'^2} = \frac{2}{3}k - 2v_t\frac{\partial u}{\partial x} \tag{3.1}$$

where

$$v_t = \frac{\mu_t}{\rho} = C_\mu\frac{k^2}{\varepsilon} \tag{3.2}$$

These equations are achieved by applying the definition of turbulent flow and using Boussinesq hypothesis in the k-ε model. Seeing that Reynolds stress should always be positive, equation 3.1 is problematic, that is when:

$$\frac{k}{\varepsilon}\frac{\partial U}{\partial x} > \frac{1}{3C_\mu} \approx 3.7 \tag{3.3}$$

The proposed solution in this model is to make C_μ sensitive to the mean flow and turbulence. The transport equation for the TKE and the equation for dissipation can be given as:

$$\frac{\partial}{\partial t}(\rho k) + \frac{\partial}{\partial x_j}(\rho k u_j) = \frac{\partial}{\partial x_j}\left[\left(\mu + \frac{\mu_t}{\sigma_k}\right)\frac{\partial k}{\partial x_j}\right] + G_k + G_b - \rho\varepsilon - Y_M + S_k \tag{3.4}$$

$$\frac{\partial}{\partial t}(\rho \varepsilon) + \frac{\partial}{\partial x_j}(\rho \varepsilon u_j) = \frac{\partial}{\partial x_j}\left[\left(\mu + \frac{\mu_t}{\sigma_\varepsilon}\right)\frac{\partial \varepsilon}{\partial x_j}\right] + \rho C_1 S\varepsilon - \rho C_2\frac{\varepsilon^2}{k+\sqrt{\nu\varepsilon}} + C_{1\varepsilon}\frac{\varepsilon}{k}C_{3\varepsilon}G_b + S_\varepsilon \tag{3.5}$$

$$C_1 = max\left[0.43, \frac{\eta}{\eta+5}\right] \tag{3.6}$$

$$\eta = S\frac{k}{\varepsilon} \tag{3.7}$$

and

$$S = \sqrt{2S_{ij}S_{ij}} \tag{3.8}$$

where G_k is the generation of turbulent kinetic energy due to the mean velocity gradients, G_b the generation of turbulence kinetic energy due to the buoyancy, Y_m the fluctuating dilatation in compressible turbulence to the overall dissipation rate. Furthermore, C_2 and C_3 are constants, σ_k and σ_ε the turbulent Prandtl numbers for k and ε and S_k and S_ε are the source terms. The form of the ε equation is much different than that of other turbulence models. One of the noticeable differences is that the production term does not contain the "k" term. The reason for this is that it is believed that the spectral energy transfer is better represented. Another difference is that the destruction term, the third term on the right-hand side of equation 3.5, does not contain any singularity (the denominator is never zero).

Eddy viscosity is computed from equation 3.9 and is employed by all the k-ε models.

$$\mu_t = \rho C_\mu \frac{k^2}{\varepsilon} \tag{3.9}$$

As previously stated, this model differs from the others by implementing C_μ and the fact that it is not constant and is calculated using the following equations:

$$C_\mu = \frac{1}{A_0 + A_s \frac{kU^*}{\varepsilon}} \tag{3.10}$$

where

$$U^* = \sqrt{S_{ij}S_{ij} + \tilde{\Omega}_{ij}\tilde{\Omega}_{ij}} \tag{3.11}$$

and

$$\tilde{\Omega}_{ij} = \Omega_{ij} - 2_{\varepsilon_{ijk}\omega_k} \tag{3.12}$$

and

$$\Omega_{ij} = \overline{\Omega_{ij}} - \varepsilon_{ijk}\omega_k \tag{3.13}$$

Where $\overline{\Omega_{ij}}$ is the mean rate-of-rotation tensor with angular velocity ω_k viewed in a rotating reference frame. The model constants A_0 and A_s are given as:

$$A_0 = 4.04 \tag{3.14}$$

$$A_s = \sqrt{6}\cos\Phi \tag{3.15}$$

$$\Phi = \frac{1}{3}\cos^{-1}(\sqrt{6}W) \tag{3.16}$$

$$W = \frac{S_{ij}S_{jk}S_{ki}}{\tilde{S}^3} \tag{3.17}$$

$$\tilde{S} = \sqrt{S_{ij}S_{ij}} \tag{3.18}$$

$$S_{ij} = \frac{1}{2}\left(\frac{\partial u_j}{\partial x_i} + \frac{\partial u_i}{\partial x_j}\right) \tag{3.19}$$

In equations 3.1 - 3.19 it can be seen that C_μ is dependent on the mean strain and rotation rates, turbulence fields and the angular velocity of the system rotation.

The other model constants are given in Table 3.1.

Table 3.1: k-epsilon mathematical constants

Parameter	Value
$C_{1\varepsilon}$	1.44
C_2	1.9
σ_k	1.0
σ_ε	1.2

3.2 Simulation geometry

The geometry length of the model was chosen to be 200 mm. This length was chosen to be easily comparable to that of an experimental set-up located in the heat transfer lab. The experimental set-up can mount a spike section of 200 mm, but differs from the actual spike concept, only containing 24 symmetrical internal fins. Thus, a spike consisting of 24 symmetrical fins should be considered. When considering any symmetrical part, only one part of the symmetry has to be simulated, which concludes that only one of the fins are to be modelled.

The geometry was modelled in Autodesk inventor 2018. The model was then imported to Ansys SpaceClaim, where the fluid and solid domains were identified. The solid domain was already present and the fluid domain was created using the built-in function volume extract and defining it as a fluid. The detailed simulation model geometry is shown in Figure 3.1.

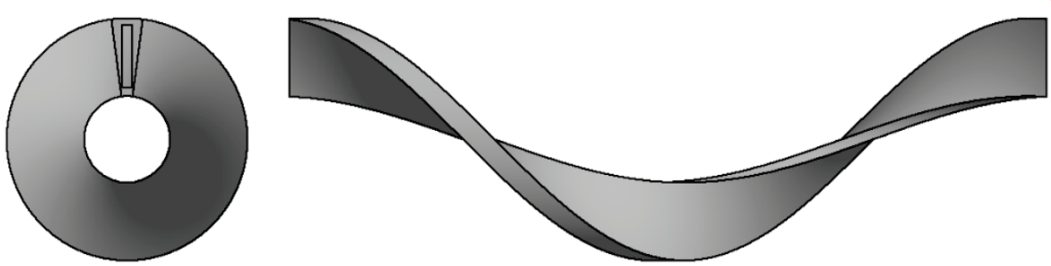

Figure 3.1: Simulation geometry

The centre of the figure shows the fluid domain through which air will flow and the outer domain shows the titanium fins section and cover (see Figure B.3 in appendix B).

3.3 Meshing method

The next step was to mesh the domains within the geometry. There are two areas, one of major concern and the other of minor concern. Three possible mesh shapes can be used namely hexahedral, cartesian and tetrahedral. Hexahedral and cartesian are very similar mesh shapes, the only difference being that Cartesian uses perfectly identical 3D cubes aligned with the cartesian coordinates, hence the name. The tetrahedral is a simple pyramid with four triangular faces. The mesh forms are presented in Figure 3.2.

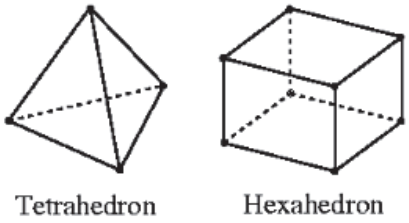

Figure 3.2: 3D Cell types

There are three possible cell arrangements available namely structured, unstructured and partially unstructured. Due to the complex geometry, a structured mesh is not ideal to use. When using the unstructured arrangement additional terms are introduced into the coefficient for the discretised equations, possibly causing it to be very large the further the cell is from orthogonal. The introduced terms cause solution dependence and create "cross-linkages".

Further these terms can reduce accuracy as well as cause solution instability. One way of avoiding these occurrences from happening is by creating a finer mesh which results in a longer computational time and a larger storage needed because of the extra cells. A partially unstructured mesh arrangement seems like the best option for this specific geometry.

The first domain that needs to be meshed is the fluid domain due to its importance. A structured mesh was created on this domain. Second, the solid titanium part was meshed using the number of divisions function to allocate a fixed number of faces to the edges of the solid. The next step was to sweep the mesh.

3.4 Simulation settings

3.4.1 General settings

The general settings define the modelling parameters accordingly. Firstly, the general simulation was set to pressure based and not density based. In both methods of solving, the velocity field is obtained from the momentum equations. The difference is that the density-based approach uses the continuity equation to obtain the density field, while the equation of state is used to determine the pressure field. The time solver was chosen to be steady state and the solver easily converged. Lastly the velocity was set to absolute seeing that there are no rotating components within the domain.

3.4.2 Models and wall treatment

For this step one should know whether laminar or turbulent flow is being dealt with. Considering high speeds, leading to a large Re, a turbulent model should be chosen. With regards to turbulent models the k-ε realizable method was chosen as stated earlier. Furthermore, the wall function approach has been chosen for this model. The solution usually deteriorates when the mesh is refined at wall surfaces when using the wall function approach but FLUENT has implemented the necessary calculation precautions to prevent this.

3.4.3 Boundary conditions

The boundary conditions were defined next. Ansys FLUENT automatically assigns a velocity inlet to the named section "inlet" where the velocity and turbulent quantities are specified. The named section "outlet" is automatically assigned an outlet pressure. Both these boundaries have fixed values (the pressure outlet only having a fixed value for sub-sonic flow). Symmetry boundaries are already set to symmetry and no added specifications are needed. The re-

mainder of the surfaces are wall boundaries set to have a no-slip condition, with the outer wall having a temperature of 100 °C and the other subject to a heat flux. A simulation 3 times as long as the test section of 200 mm was also investigated. This was done to compare the shorter domain to a longer domain in order to see what the effects of the entrance region was. The result yielded that there are no significant differences and thus the shorter domain is be used for further discussion.

3.4.4 Solution methods

The next step is to define the solution methods used in the simulation. The SIMPLE algorithm was chosen as solution method. It is a slower solver with a larger time cost, but converges easily while assuring accuracy and a convergent solution with few requisites. The least square cell based method is chosen for the calculation of the gradient terms. This method assumes the solution varies linearly and is a cell-centred scheme, has a much lower computational time than Green-Gauss-Node based and yields a higher accuracy for flow solutions. For the pressure interpolation scheme the PRESTO! scheme was used because of the high-speed rotating flow and strong curved domains present in the simulation.

All the other solution methods are set to be second-order-upwind. A second-order-upwind method achieves its accuracy though expansion of the Taylor series of the cell centred solution around the cell-centroid. The face value is calculated using the equation below:

$$\Phi_{f,SOU} = \Phi + \nabla\Phi \cdot \overrightarrow{r} \tag{3.20}$$

where Φ is the cell centred value, $\nabla\Phi$ the cell centred value's gradient in the upstream cell and $\overrightarrow{r}$ the displacement vector from the upstream cell centroid to the face centroid. This solution requires the determination of the gradient $\nabla\Phi$ in each cell and it is limited so that no new minimum or maximum are introduced.

3.4.5 Solution monitoring

Several monitors were created to track the convergence of the simulation. A velocity magnitude monitor was created on the outlet plane to track the velocity fluctuation. This was done to determine whether the flow is steady. The monitor was set to plot and write every time step.

3.4.6 Initialisation

In the last step the initialization process was performed utilizing the "hybrid initialization" method. This method solves Laplace's equation to determine the

initial pressure and velocity parameters for the iterative process. The other parameters are taken as the standard programmed values or the predefined values.

3.5 Simulation and analytical results comparison

3.5.1 Mesh independence

Curved duct

Before the results can be discussed the mesh independence had to be proven. Five different meshes were utilised to establish whether there is mesh independence in the curved duct simulation. The meshes were checked in terms of mesh size and the computational time. Two course, one medium and two fine meshes were used, with the fine meshes having up to 3 000 000 and 2 000 000 cells, the medium mesh 1 000 000 and the course meshes 500 000 and 250 000. The local wall heat transfer coefficients at the inner and outer flow area were used to investigate and establish the independence. Table 3.2 shows the detail of each mesh used during the mesh independence study. Two detailed views containing a section of the mesh can be seen in Figures 3.3 and 3.4. The mesh down the length of the fluid domain is shown in Figure 3.5.

Table 3.2: Curved duct simulation mesh details

Mesh nr	Cells $\times 10^3$	Faces $\times 10^3$	Nodes $\times 10^3$
1	272	859	313
2	499	1551	553
3	937	2889	1014
4	1973	6032	2084
5	2924	8908	3059

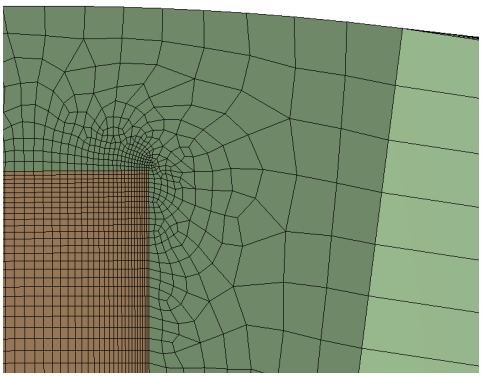

Figure 3.3: Partial view of mesh at inlet

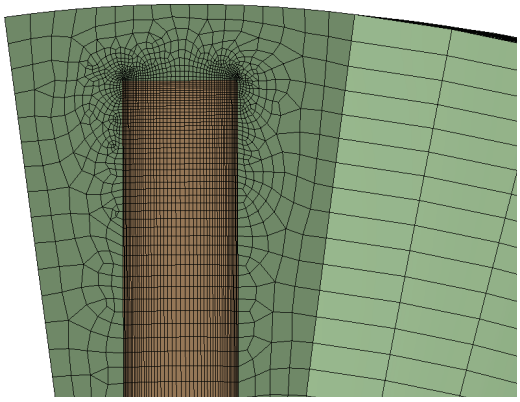

Figure 3.4: Detailed view of mesh at inlet

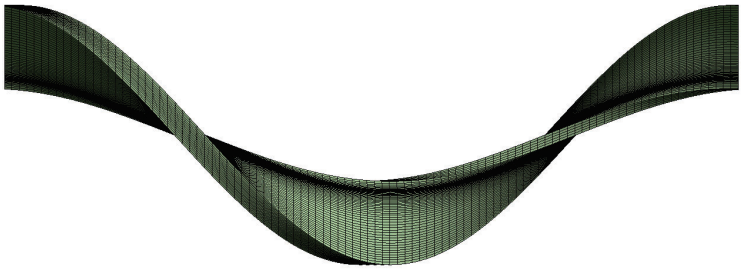

Figure 3.5: Side view of mesh

Figure 3.6 and 3.7 show the heat transfer on the inner fluid and outer fluid surface from inlet to the outlet of all the meshes. A difference of less than 1% is seen between mesh 4 and 5, thus mesh independence is proven. For computational reasons mesh 4 was used, and its results will be used in further

discussions. The exact average error difference in the wall heat transfer between all the above mentioned meshes with regard to the finest mesh (mesh 5) is shown in Table 3.3.

Table 3.3: Average error difference in wall heat transfer

Mesh nr	Inner Fluid Surface [%]	Outer Fluid Surface [%]
1	14.8	18.0
2	8.01	13.01
3	1.19	7.17
4	0.526	0.232

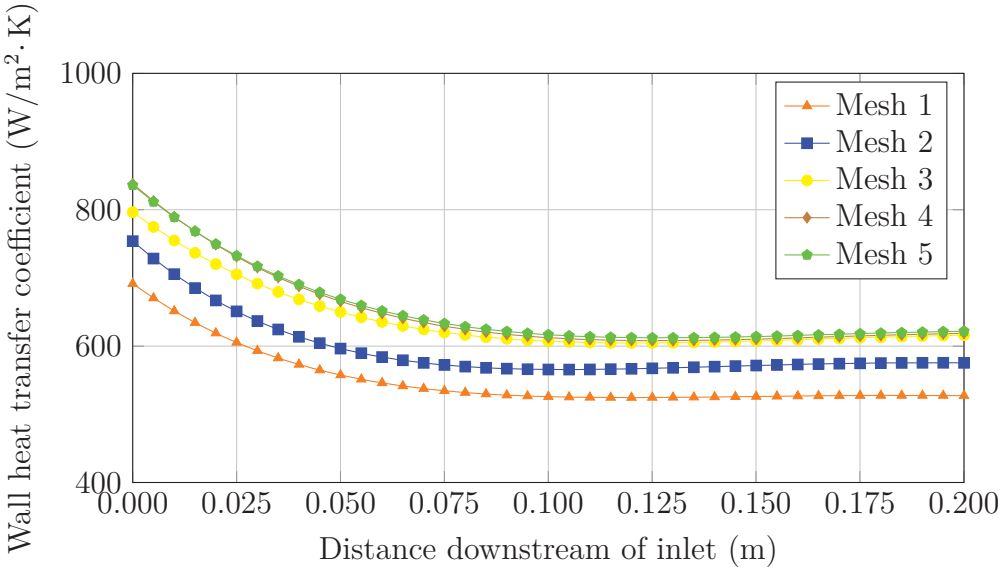

Figure 3.6: Heat transfer on the inner fluid surface

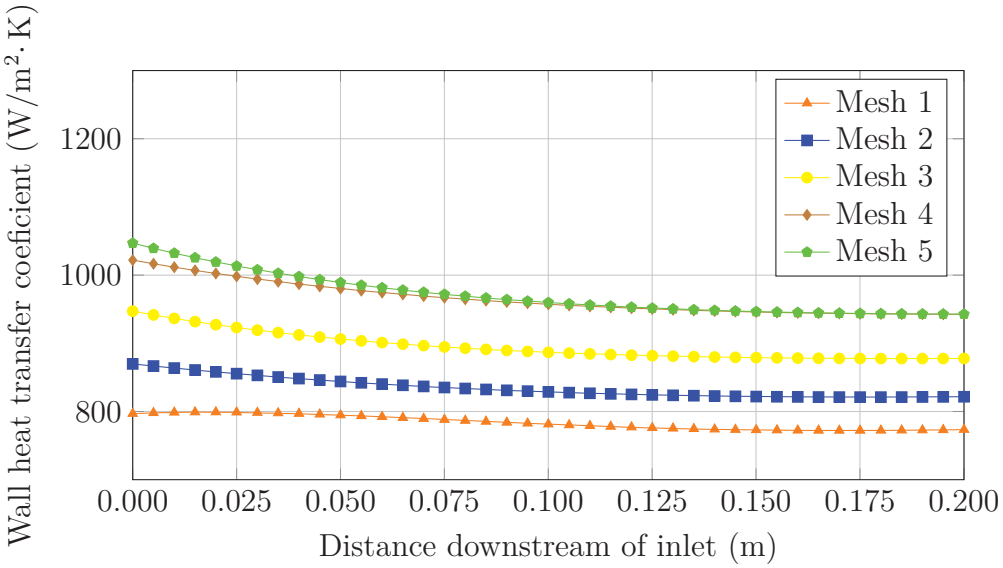

Figure 3.7: Heat transfer on the outer fluid surface

Y-plus

The turbulence models in ANSYS CFD are y^+ dependent. Bearing this in mind it is important to select an appropriate wall function which is highly dependent on the relative extent in the flow or the level of refinement in the wall neighbouring mesh. When using a standard wall function it is assumed that the log-law is applicable for the entire boundary layer region of the mesh.

The scalable wall function offers the most suitable solution, bypassing the arbitrary refinement of grids. It practically displaces the mesh to generate a y^+ value of 11.225 which is the transition to the log-law composite layer. This is done regardless of the mesh refinement level, thus bypassing the inaccurate modelling of the buffer region.

In the y^+ analysis, Figure 3.8, it can be seen that the mesh y^+ value, as predicted, with increased level of refinement strives to 11.225.

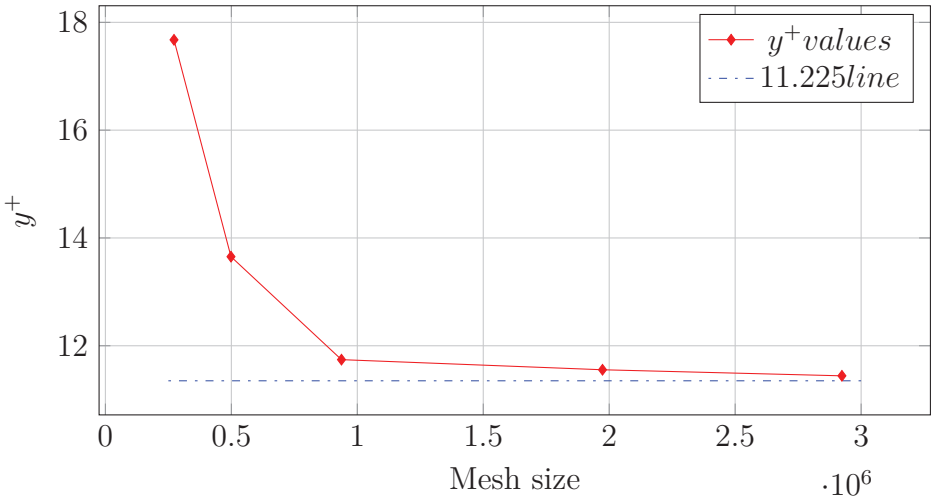

Figure 3.8: y^+ over mesh size

Straight duct

The straight duct simulation grid independence study was done using five meshes. Details concerning the mesh is shown in Table 3.4. The same meshing method used for the curved duct simulation was followed in the straight duct simulation. Further details on the mesh independence of the straight duct simulation can be found in Table 3.5, where the average error difference in heat transfer with regard to the finest mesh is shown and in Appendix A, where several graphs providing the necessary motivation for the independence study is presented.

Table 3.4: Straight duct simulation mesh details

Mesh nr	Cells $[\times 10^3]$	Faces $[\times 10^3]$	Nodes $[\times 10^3]$
1	80.9	256	93.8
2	166	516	184
3	277	856	301
4	633	1936	670
5	811	2474	852

Table 3.5: Average error difference in wall heat transfer for straight duct simulation

Mesh nr	Inner Fluid Surface [%]	Outer Fluid Surface [%]
1	17.5	17.6
2	12.3	13.1
3	8.65	8.47
4	0.145	-0.0537

For computational reasons mesh 4 was used for further calculations and discussions.

3.5.2 Results

The following section contains a detailed discussion of the results obtained in the numerical simulation.

Effect of different flow rates

To better understand the influence the swirl in a duct has on the heat transfer rate, different mass flow rates had to be investigated. The results obtained is summarized in Table 3.6.

Table 3.6: Different mass flow rates effect on heat transfer and pressure drop

Mass flow rate	Parameter	Unit	Straight duct	Curved duct
0.004 (kg/s)	Average heat transfer coefficient	$[W/m^2K]$	204	258
	Max heat transfer coefficient	$[W/m^2K]$	224	285
	Min heat transfer coefficient	$[W/m^2K]$	181	196
	Pressure drop	$[Pa]$	135	199
0.0665 (kg/s)	Average heat transfer coefficient	$[W/m^2K]$	332	419
	Max heat transfer coefficient	$[W/m^2K]$	355	473
	Min heat transfer coefficient	$[W/m^2K]$	280	307
	Pressure drop	$[Pa]$	202	525
0.093 (kg/s)	Average heat transfer coefficient	$[W/m^2K]$	453	575
	Max heat transfer coefficient	$[W/m^2K]$	491	677
	Min heat transfer coefficient	$[W/m^2K]$	354	409
	Pressure drop	$[Pa]$	327	991
0.1195 (kg/s)	Average heat transfer coefficient	$[W/m^2K]$	479	728
	Max heat transfer coefficient	$[W/m^2K]$	525	867
	Min heat transfer coefficient	$[W/m^2K]$	424	509
	Pressure drop	$[Pa]$	479	1594
0.146 (kg/s)	Average heat transfer coefficient	$[W/m^2K]$	657	878
	Max heat transfer coefficient	$[W/m^2K]$	744	1021
	Min heat transfer coefficient	$[W/m^2K]$	489	608
	Pressure drop	$[Pa]$	569	2732

Heat transfer

The heat transfer rate in a straight duct is the same on the inner and outer flow surface because no secondary flow or swirl effects are present. In Figure 3.9 a graph comparing the heat transfer rate of a curved duct versus a straight duct is shown. The heat transfer rate is nearly double at the outer wall of the curved duct and 20 - 30 % more on the inner surface. This proves theory discussed in Chapter 2 where the outer surface will experience higher heat transfer than the inner surface of a curved duct.

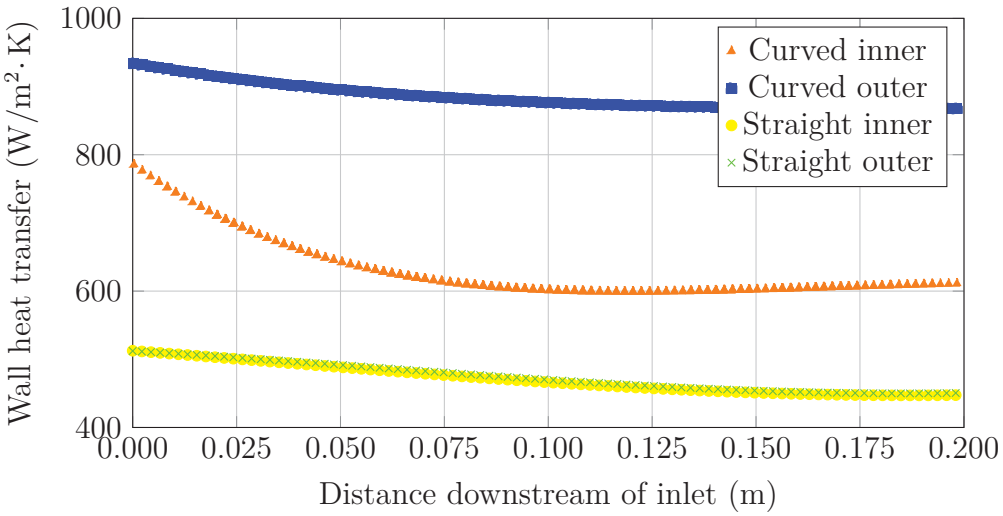

Figure 3.9: Heat transfer (curved duct over straight duct)

In both cases the heat transfer rate starts high and then decreases to a certain constant. This is due to the high turbulence, also known as the entrance effect, experienced at the inlet of the duct. As the turbulence dies down, the heat transfer rate reduces. It is important to note that the heat transfer at the outer surface of the curved duct does not decrease as much. This is due to the secondary flow constantly inducing turbulence.

The average heat transfer coefficient at different flow rates are shown in Figure 3.10. There is a clear indication that the heat transfer coefficient is higher in the curved duct simulation with a maximum increase of 34 % at a mass flow rate of 0.146 kg/s (Re = 32 000). The heat transfer coefficient increases with the increase in mass flow rate, making the largest mass flow rate simulated the maximum point of heat transfer coefficient increase.

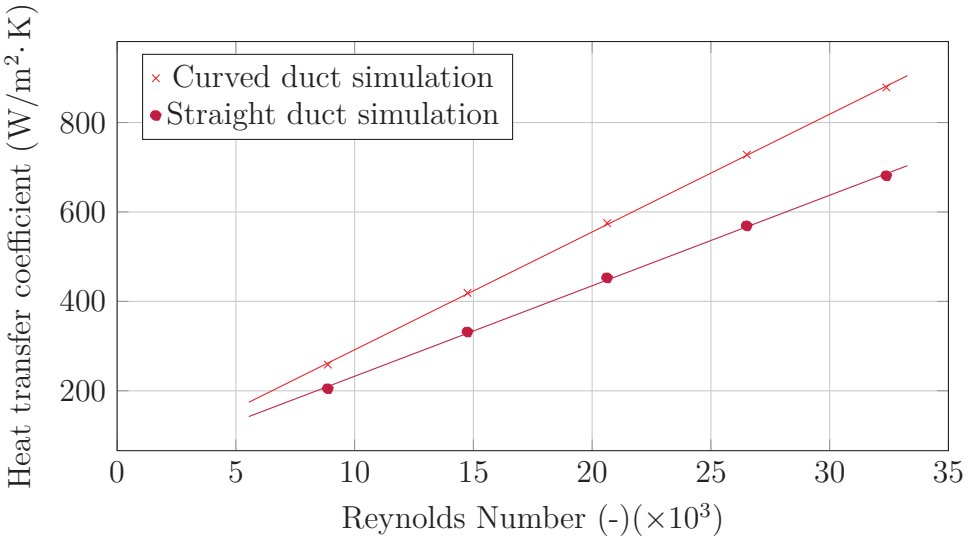

Figure 3.10: Straight duct simulation over curved duct simulation results for heat transfer at different Reynolds numbers

Pressure drop

The increase in heat transfer comes at a cost of pressure drop. This pressure drop is due to the extended surface contact time and friction between the fluid and fin walls. The pressure drop can be quantified in terms of the friction factor and converted to pascals as stated in Chapter 2.

In Figure 3.11 the pressure drop of a straight duct versus the curved duct in the specific simulation conditions is shown. The pressure drop is exponential in nature for both simulation results. However, the curved duct simulation is significantly higher than the straight duct simulation at higher flow rates, with more than a 200 % increase at Reynolds number of 32 500 for the simulated distance of 200 mm.

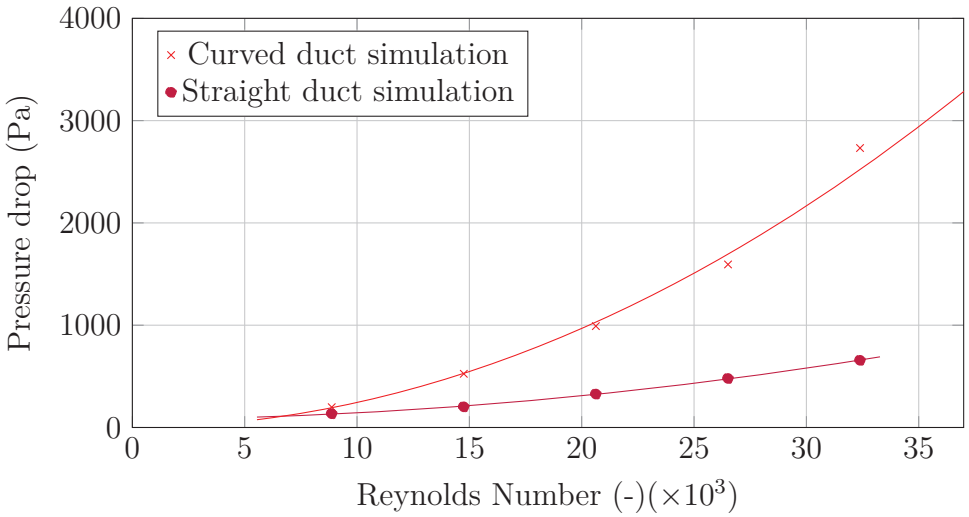

Figure 3.11: Straight duct simulation over curved duct simulation results for pressure drop at different Reynolds numbers

Secondary flow manifestation

Contributing to the increase in heat transfer is the secondary flow patterns. Figure 3.12 and 3.13 shows the secondary flow present a 100 mm downstream of the inlet. The centrifugal force exerted on the fluid forms small vortices close to the outer wall causing the increase in heat transfer.

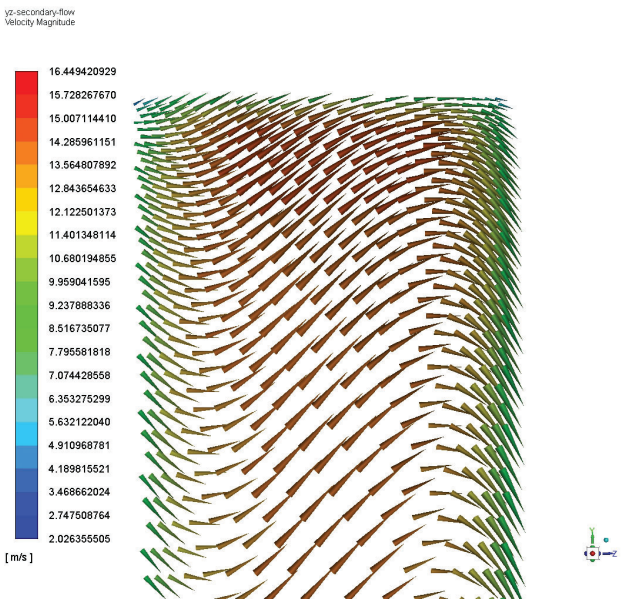

Figure 3.12: Secondary flow patterns for the top section of the helical duct 100 mm downstream of the inlet

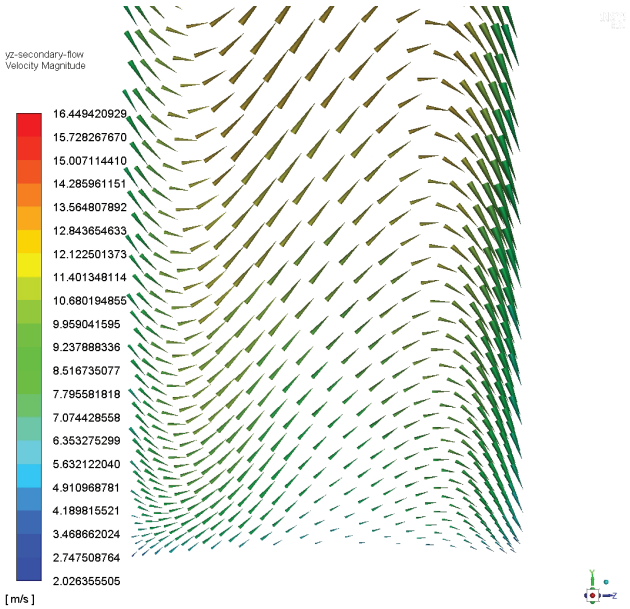

Figure 3.13: Secondary flow patterns for the bottom section of the helical duct 100 mm downstream of the inlet

3.6 Comparison of theoretical and simulation results

The next step is to compare the simulation results to the theoretical results. In both simulation the material was also taken to be titanium to be comparable to each other. This changed the heat transfer results of the straight duct simulation significantly compared the results in the study by Lubkoll *et al.*. The heat transfer results obtained by the simulation is thus strictly for comparison to the curved simulation and theoretical results discussed. Further, the temperature distribution within the fins for the curved simulation is shown in Figure 3.14.

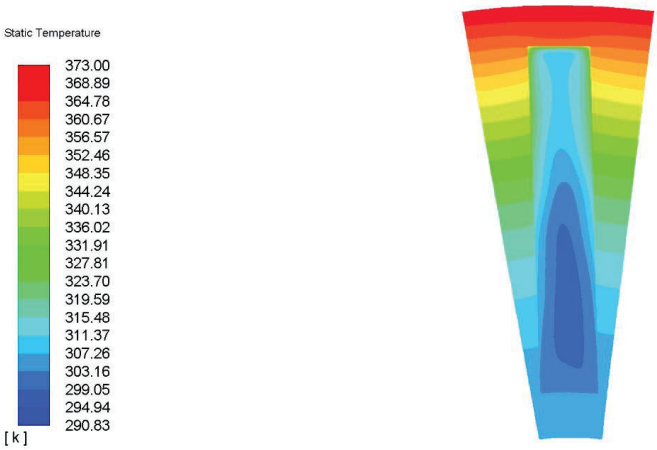

Figure 3.14: Temperature distribution within the fin

3.6.1 Heat transfer

In Figure 3.15 both simulation results as well as theoretical results are shown for comparison reasons. It can be seen that the straight duct simulation's heat transfer coefficient at low Reynolds numbers are well predicted by the theoretical correlation. However, it is noticeable that at higher Reynolds numbers the heat transfer coefficient is higher than theoretically predicted. The average difference is 14.8 %. This may be a result of the duct's unique thin and long geometry, thus the correlations where never proven for such geometries.

The heat transfer coefficient of the curved duct simulation is close to Kakac *et al.* correlation but not a precise match, with an average difference of 14.3 %. Once again the difference could be due to the unique geometry of the duct not being accounted for during the derivation of the correlations.

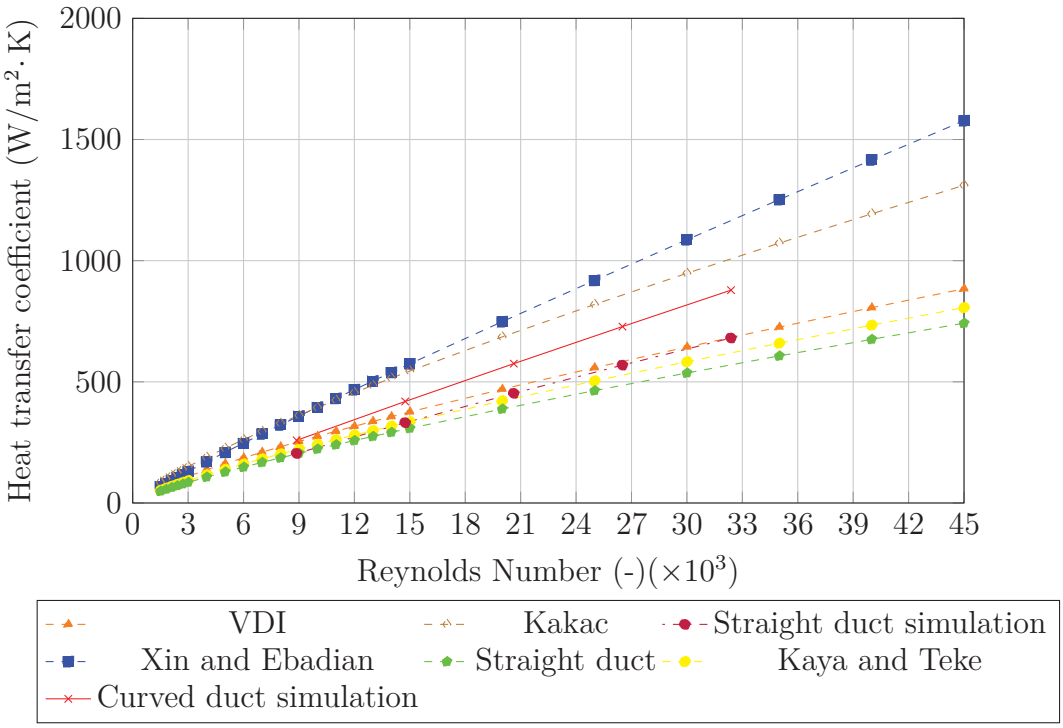

Figure 3.15: Heat transfer over Reynolds number

3.6.2 Pressure drop

Figure 3.16 shows the comparison of the simulations and the theoretical results for the pressure drop for the given geometry. The pressure drop of straight simulation follow the theoretical straight duct results well, only deviating a small amount towards the higher flow rate region. The pressure drop of the simulation has an average deviation from the theoretical results of 7.5%.

The curved duct results correlate well with both the VDI and Kakac methods for calculating the pressure drop. It differs a maximum of 11.2 % from the VDI method and 12.2 % from Kakac's method. The correlations predict the pressure drop better at lower Reynolds numbers with Kakac and the VDI predicting within an average of 4 % in the range of $5000 < \mathrm{Re} < 27\,500$.

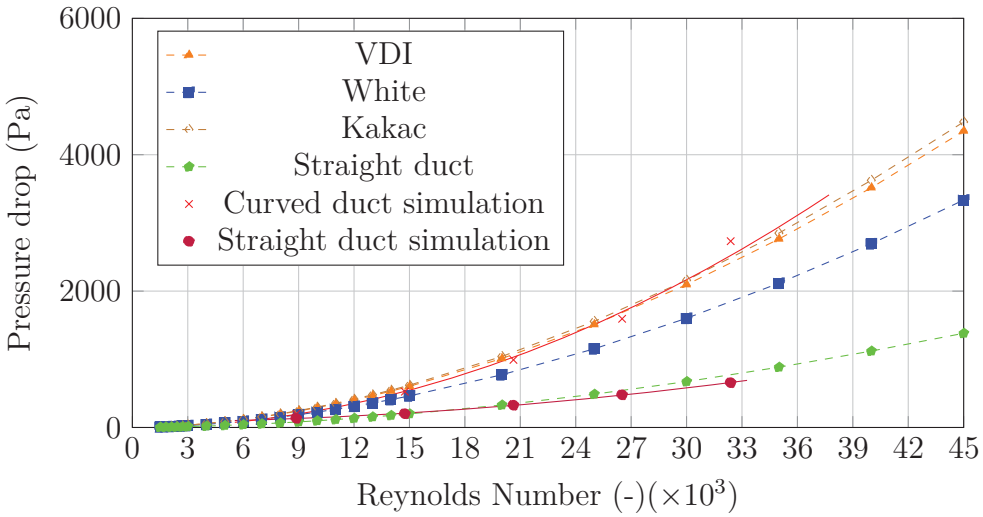

Figure 3.16: Pressure drop over Reynolds number

3.7 Conclusion

In conclusion the simulation correlates with the theoretical pressure drops, with an average difference of 4 % at low to mid Reynolds numbers with some larger deviations in the high flow region. Furthermore, the heat transfer coefficient's deviation of the simulations and theoretical results are on average 14 %. This is relatively large in comparison to the pressure drop prediction. Nonetheless, the curves have the same trend which is insightful and important for further investigations.

The heat transfer coefficient increases between 20 - 30 % with the implementation of a curved duct. However, the pressure drop increases with more than 100 % at high Reynolds numbers.

Taking all this into account, experimental testing will contribute to better understanding the investigated effect of helically swirled fins and where possibilities for improvements are.

Chapter 4

Experimental set-up

In this chapter the experimental set-up is introduced as well as discussions around the design, measuring equipment, functionality and the error and uncertainty of the experiment.

4.1 Experimental set-up

The experimental set-up was designed by Lubkoll (2017). It was constructed and built in the heat transfer lab situated in the mechanical department of the engineering faculty of Stellenbosch University. The set-up was designed to be interchangeable, permitting the testing of different spike components in multiple configurations. The initial configuration of the set-up was configured to measure the pressure drop and heat transfer within ducts of rectangular cross-sections. Initial objectives of the set-up were to validate an air flow and pressure model and a heat transfer model.

The set-up was designed to operate with steam as a constant temperature heat source. This is achieved through the steam providing a constant surface heating temperature of nominally 100 °C.

The design should be able to withstand the maximum pressure of 10 bar. The pressure exceeds 50 kPa with a nominal diameter of 70 mm thus the modified part falls under the pressure vessel safety regulations of SANS and the "Categorization and conformity assessment criteria for all pressure equipment". This specific design falls into group 2 of the SANS 347 classification (Figure C.1). The wall stress in the tangential direction in a cylinder pressure vessel is described as:

$$\sigma_t = \frac{Pr}{t} \tag{4.1}$$

where P is the pressure, r is the radius and t is the wall thickness of the vessel. With the maximum conditions applied (P = 10bar, t = 2 mm and r = 0.035 m)

it amounts to a result of $\sigma_t = 15.75\,\text{MPa}$.

This case, as above with parameters p = 10 bar and r = 35 mm and a wall thickness t = 2 mm has been configured in MSC patran with a maximum temperature of 100 °C for worst case scenario to be present. A 7.5 ° slice of the tube was meshed and the edge pressure boundary condition applied. As a result the inner wall stress σ_t was given with 15.7 MPa, correlating well with the analytical solution of 15.75 MPa calculated using the above equation.

The FEM analysis on the stress concentration in the corner shows a stress of 810 kPa, shown in Figure 4.1. This is due to the simulation geometry being made to be the worst-case scenario. The corner radius is taken to be 0.08 mm, this is the smallest it can possible be due to the laser sintering 3D printer's capabilities. Even when this high stress is considered the material strength will be sufficient with a tensile strength of 1000 MPa.

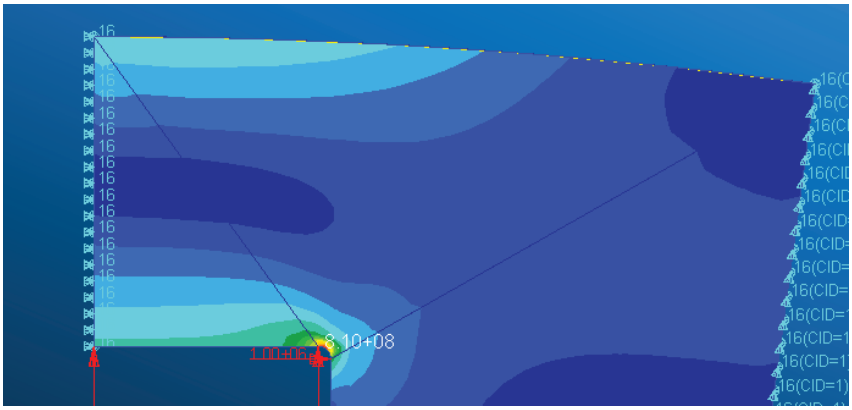

Figure 4.1: Stress concentration point

.

4.2 Design

The experimental test set-up was constructed around the steam chamber which heats the finned test section. The initial internally finned tube is shown in Figure 4.2 with multiple thermocouples and pressure taps shown along the edges of the cylinder.

In Figure 4.2 an extra straight finned section is shown. This section is completely insulated with thermal cladding and is present in the system to assist the flow to stabilize and develop before entering the specific test section.

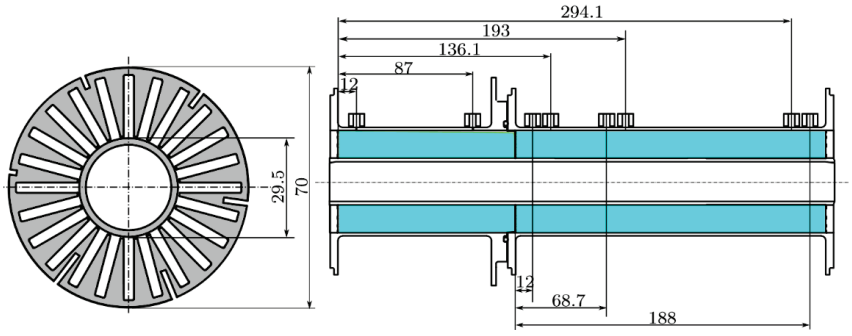

Figure 4.2: Internally finned tube section with different depths of thermocouples ranging from 2.0 mm - 10.4 mm (left), axial positions of pressure taps above tube, axial distance of thermocouples below tube (right) (Lubkoll, 2017)

In Figure 4.3 a photo of the test section with thermal insulation cladding is shown with the steam chamber intact. The steam chamber has its own independent mounting. Thus, it is attached separately and sealed with a silicone gasket foam at the flange end insulating the test section from conduction towards the wall. This independent mounting is fastened to a 1m long rail which allows the steam chamber to move in an axial direction, further ensuring interchangeability of the system. The steam chamber is insulated using an outer steam cavity forming a steam jacket, as seen in Figure 4.4. No extra insulation is needed for the steam chamber.

Figure 4.3: Heated test section with steam jacket and insulation (Lubkoll, 2017)

In the heated section multiple interchangeable tubes are present to allow the removing of tubes, modification of test sections and other design changes to be possible. A real spike consists of three parts namely the inner tube, the internally finned outer tube and the end cap/spike tip. In both cases air travels through the inner tube towards the spike tip where it is redirected by 180 °. In the test set-up air then enters the annular section where the wall friction is stabilized and the flow is allowed to fully develop before passing through the heated test section.

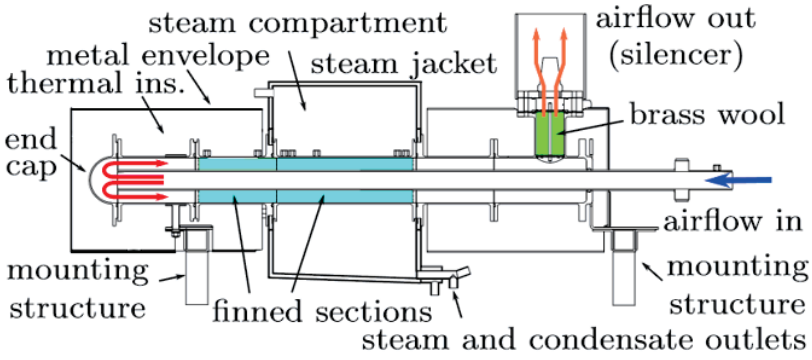

Figure 4.4: Heated test sectioned view (Lubkoll, 2017)

The flange is thermally insulated using 2.5 mm thick gaskets, creating an air gap towards the internally finned test section situated in the steam compartment. On the other side of the internally finned section, the opposing flange is insulated using the same 2.5 mm thick gasket. Heated air then flows through another identical annulus segment towards the last segment. In the last segment the air is redirected 90 ° upwards through brass wool towards the silencer. The brass wool serves to mix the air, on the condition that it should be stratified, to achieve a more homogeneous air temperature.

A flange is positioned near the air exit point around the silencer which houses three thermocouples, each inserted at different depth to accurately measure the outlet temperature of the air.

An orifice plate, shown in Figure 4.5, is present at the start of the set-up to compute the mass flow rate and the system pressure using a differential pressure and gauge pressure sensor respectively. Prior to the air entering the test set-up, a second device measures the static pressure drop over a distance of 0.5 m along the inner tube. This static pressure drop can be used to compute the mass flow rate, assuming the flow is fully developed. The purpose of this secondary device is to verify the orifice plate calculation.

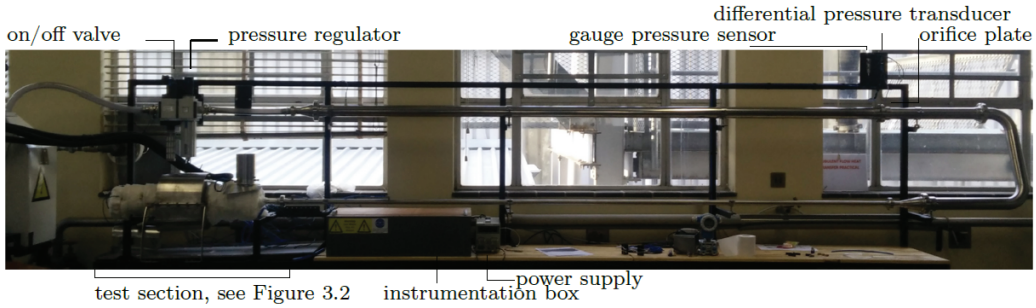

Figure 4.5: Full test set-up (Lubkoll, 2017)

In Figure 4.5 a steam generator can be seen on the left-hand side. This is one of two steam generators that are active in the system, one supplying steam to the steam compartment and the other supplying steam to the metal envelope. Above the test section in Figure 4.4 an on/off valve and pressure regulator are situated to control the air flow from the air supply.

The inlet pressure and inlet air flow velocity can be computed by taking the differential pressure reading between the static pressure tap 15 cm upstream from the start of the test section and the gauge pressure sensor at the orifice plate. Connected to this pressure tap is an air distribution manifold which serves as reference to all downstream pressure taps in the test section. Pressure taps are located at different axial positions within the finned section, shown in Figure 4.2, where they are uniformly spaced by 120 °.

There are two finned sections joined together, one straight duct section for the purpose of developing the flow and the other a swirled duct section within the steam chamber for testing purposes. The duct geometry of both these sections are the same with a width of 3 mm, an outer diameter of 70 mm, a wall thickness of 2 mm and an inner diameter of 30 mm. Figure 4.6 shows the dimensions of one of these ducts.

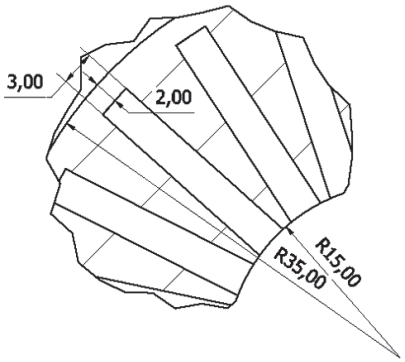

Figure 4.6: Rectangular duct dimensions

In the spike there are 24 of these rectangular ducts equally spaced and rotating one full turn within the test length of 200 mm. Some detail on the part and its manufacturing is shown in Appendix B. The corners of the ducts are considered stress hot spots, having a radius of 0.08 mm. Though this is small the strength of the material easily overcomes this stress concentration as shown in the FEM analysis below.

Directly measuring the air temperature is challenging with the narrow width of the duct. Thus, six thermocouples are inserted at different depths, ranging from 2 mm - 10.4 mm into the fins to increase the quality and amount of information available on the heat transfer within the test section. This is done a total of three times in the axial distance. The positioning in the axial direction is visible in Figure 4.2. Furthermore, three thermocouples, equally spaced are inserted at the same depth, 7.04 mm, at two axial locations to gather information on the heat transfer symmetry within the test section.

4.3 Instrumentation

Gauge pressure sensor
The gauge pressure sensor already in place is a Firstrate FST800-10B pressure sensor with the specifications listed in Table 4.1.

Table 4.1: Firstrate FST800-10B gauge pressure sensor specifications

Parameter	Value	Unit
Pressure range	0 - 100	kPa
Supply voltage	9 - 30	VDC
Signal output	4 - 20	mA
Accuracy range $e_{p_1,1}$	0.3	%
Zero drift	0.02	%/°C
Thermal sensitivity shift	0.02	%/°C

Differential pressure transducer

The differential pressure transducer presently incorporated in the set-up is a Freescale MPX205DP with the specifications shown in Table 4.2.

Table 4.2: Freescale MPX2050DP differential pressure transducer specifications

Parameter	Value	Unit
Pressure range	0 - 50	kPa
Supply voltage	10 - 16	VDC
Signal output	0 - 40	mV
Linearity $e_{\triangle p,1}$	0.25	%
Pressure hysteresis $e_{\triangle p,1}$	0.1	%

Data logger

During the experiments data had to be collected. This was done by the use of a data logger. The specific data logger used in the experiments is a keysight 34998A. Specifications on the data logger is given in Table 4.3.

Table 4.3: Keysight 34998A data logger specifications

Parameter	Value	Unit
100 mV range		
Range error $u_{L,0}$	0.004	%
Accuracy in reading $e_{L,1}$	0.005	%
100 mA range		
Range error $u_{L,0}$	0.005	%
Accuracy in reading $e_{L,1}$	0.05	%

Chapter 5

Experimental validation, method and results

In the following chapter the applicability as well as the error and uncertainty is discussed. Further this chapter contains the method on how the experiments were conducted combined with a discussion on the detailed analysis of the experimental results. The method of experimentation is made to be similar to the study done by Lubkoll *et al.* (2016).

5.1 Calibration

Each one of the T-type thermocouples was calibrated by using the FLUKE 9142 dry well calibrator. Each thermocouple has an individual curve suited for just that thermocouple. The calibration was done by taking measurements in 10 °C intervals from 20 °C - 100 °C. An accuracy better than 0.1 °C is achieved with the calibration curves.

The pressure transducers were calibrated using a Betz micromanometer with a range of up to 5000 Pa in 500 Pa increments. The gauge pressure sensor was calibrated using a master pressure gauge ranging from 0 - 10 bar in increments of 100 kPa. More detail on the calibration and the accuracy achieved are shown in Appendix D.

5.2 Possibilities for errors

The calibrations done on the pressure transducers allow for a very high accuracy. However, there are several effects that that are difficult to quantify and account for. The zero-drift is one of these effects being notable at lower pressures when various pressures over different time durations are introduced. The measurement uncertainty is calculated as the root-mean-square of the

zero-order uncertainty of each device and the root-mean-square of its elemental errors. The equation used to calculate the uncertainty is shown in equation 5.1.

$$u_d = \pm\sqrt{u_0^2 + u_x^2} \tag{5.1}$$

The instrumental errors are generally provided from a data sheet where the value of u_0 of half the instrument resolution is used. The devices and their uncertainties are:

- The pressure transducer errors are given as $e_{\Delta p,1} = 0.25\,\%$ linearity error and $e_{\Delta p,2} = 0.1\,\%$ pressure hysteresis (Freescale, 2008). The temperature hysteresis errors are not considered seeing that the drop in pressure that is measured over the orifice is at ambient/room temperature. Thus, $u_{d,\Delta p} = \pm\sqrt{e_{\Delta p,1}^2 + e_{\Delta p,2}^2} = \pm\sqrt{0.25^2 + 0.1^2}\,\% = \pm 0.269\,\%$. The data sheet provided with the data logger shows a range error of $u_{L,0} = \pm 0.004\,\%$ and an accuracy in reading error of $e_{L,1} = \pm 0.005\,\%$ (Keysight Technologies, 2014). The measurement range is 0 - 100 mV thus making $u_{L,0} = \pm 0.004\,mV$.
- The firstrate FST800-10B pressure sensor error is provided as $\pm 0.3\,\%$ at full-scale of 1000 kPa. As for the measurement uncertainty, $u_{p1,d}$ is computed with the data acquisition system error. The signal output is in ampere and ranges from 4 mA - 20 mA. The range error $u_{L,0} = \pm 0.005\,\%$ with an accuracy in reading error of $e_{L,0} = \pm 0.05\,\%$ for an ampere reading range of 0 mA - 100 mA (Keysight Technologies, 2014).

5.3 Experimental method

Figure 5.1 and 5.2 shows the typical procedures by showing the pressure drop of the pressure transducer and the pressurized air stream inlet and outlet temperatures. The data logging is done through continuous logging in four second intervals.

Step 1: Zero reading

Before starting the experiment, a set of zero readings is taken for all devices. This data will later be used to determine whether the zero-drift affects the results.

Step 2: Stabilization

The compressor is situated approximately 20 m from the test set-up. The pipes supplying the air to the set-up are located outside, exposed to ambient air and weather conditions (uninsulated). This can cause a temperature deviation in the available air to air supplied directly after flow is initiated. For this reason,

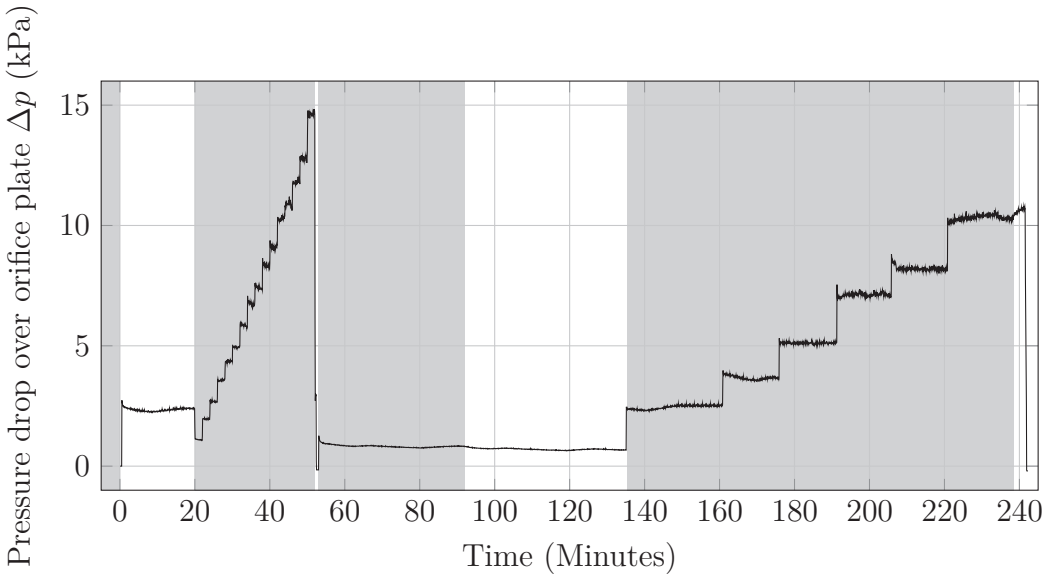

Figure 5.1: Pressure drop over orifice in a complete cycle

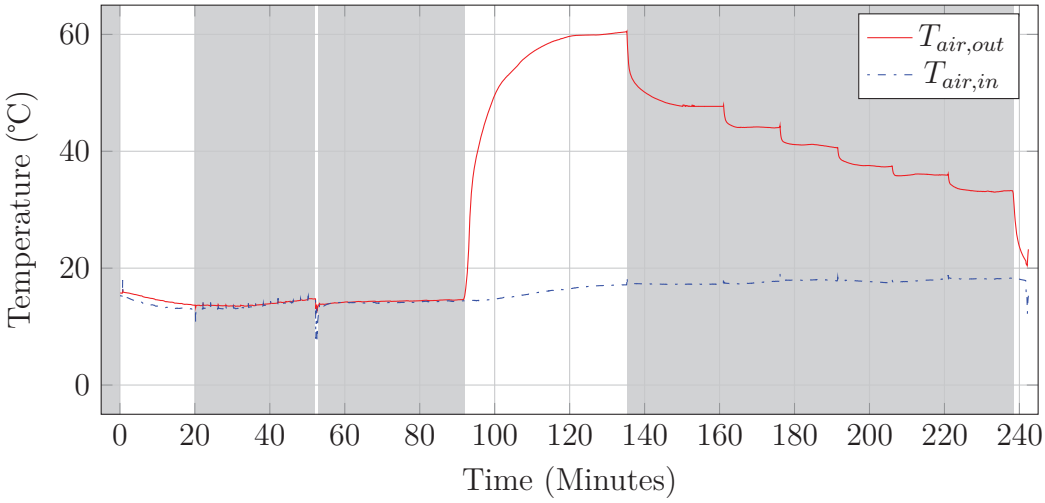

Figure 5.2: Air inlet and outlet temperatures in a complete cycle

the air is allowed to flow for several minutes thus stabilizing the air inlet temperature.

Step 3: Pressure test
The pressure regulator is manually activated, adjusting the inlet air pressure in approximately 50 kPa intervals to increase the air flow rate through the set-up. Each pressure interval is kept constant for approximately 2 minutes to gather a set of data point, which is averaged to gain the exact pressure at the set point.

Step 4: Zero reading
The air flow is then turned off and the set-up is pressurized. Step one is repeated, gaining another set of zero readings for the zero-drift analysis.

Step 5: Heating
After the zero readings are taken the air supply and steam generators are activated. Steam floods the steam compartment after 90 minutes and the outlet temperature rises rapidly. The heated air expands thus causing a slight drop in mass flow rate as the air stream is regulated via a pressure regulator which maintains a constant inlet pressure. The inlet pressure is then kept constant until steady state can be assumed.

Step 6: Varying flow rates
The next step is to vary the flow rates. Air flow rates are increased by increasing the inlet pressure, this is done in intervals of approximately 100 kPa. Temperatures are, as in step 5, observed until they reach steady state.

The temperature increased with 6 °C during the course of this test cycle, this is due to the test starting during the early morning and as a result the temperature increases towards noon. At the start of the test the air is hot and cools down to stabilize after about 15 minutes. This hot air was the air trapped within the 20 m pipe section as well as the air that cooled down the slightly heated pipe section. The spikes in the inlet temperature in Figure 5.2 are caused by the sudden pressure increase when adjusting the inlet pressure.

With the increase in mass flow rate, an increase in thermal power is needed. The supply voltage of the steam generators is adjusted manually. Observation of the steam temperature readings and steam flow from the steam compartment's outlet indicate whether the steam flow rate is sufficient for the current air flow rate. The steam generators' supply voltage is adjusted manually to avoid pressure building up in the steam system and consequently reach temperatures higher than 100 ℃.

Step 7: Shut down

In the last step the steam generators are turned off. This is done after the last steady state readings have been logged. As the air temperature decreases, the pressure drop increases due to the shrinkage of air consequently increasing the mass flow rate while keeping the inlet pressure constant. Another set of readings are taken after the air flow supply is turned off, contributing data to the zero-drift analysis. The outlet temperature is observed to be increasing due to the mounting flange which was heated via conduction along the sheath.

5.4 Data preparation

To present the data for comparison a detailed analysis of the data is needed. The readings taken for the pressure increase stage of testing is done by taking the average pressure and calculating the mean values, whilst inspecting for irregular behaviour. The voltage reading taken by the data logger is converted to pressure (differential pressure) by applying the calibration curves calculated for each individual pressure transducer. The gauge pressure sensor's ampere reading is converted to kPa gauge pressure. The ambient pressure is acquired, after a successful execution of the experiment, from the university's weather station. Each thermocouple has a corresponding calibration curve which corrects the reading to an accuracy of less than 0.1 °C.

The air flow rate is determined using an orifice plate. The orifice plate calculations are based on the measurement of fluid flow in closed conduits (British Standard, 1993). The air flow rate is determined using the static pressure drop over the orifice plate. The device within the test set-up is shown in Figure 5.3, describing all the parameters used to calculate the mass flow rate.

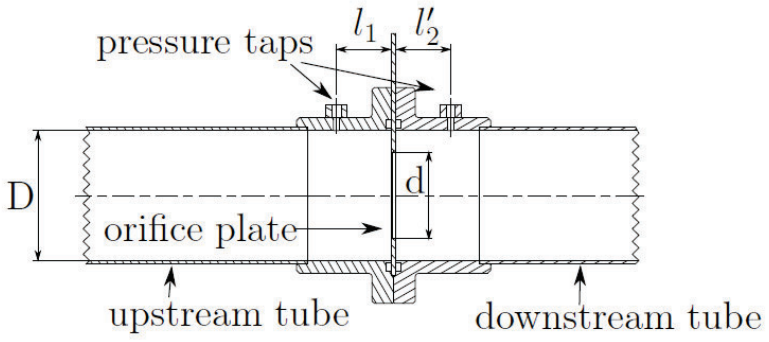

Figure 5.3: Orifice plate with dimensions (Lubkoll *et al.*, 2016)

The mass flow rate is calculated using equation 5.2

$$\dot{m}_{air} = CE\varepsilon\frac{\pi}{4}d^2\sqrt{2\Delta p \times \rho_1} \tag{5.2}$$

where C, the coefficient of discharge is:

$$C = 0.5959 + 0.0312\beta^{2.1} - 0.1840\beta^8 + 0.0029\beta^{2.5}\left[\frac{10^6}{Re_D}\right]^{0.75} + 0.0900L_1\beta^4(1-\beta^4)^{-1} - 0.0337L_2'\beta^3 \tag{5.3}$$

where $L_1 = l_1/D$ where l_1 is the distance of the upstream pressure tap to the upstream face of the orifice plate and $L_2' = l_2'/D$ in the same way is the distance of the downstream pressure tap to the downstream face of the orifice plate.

$$E = (1-\beta^4)^{\frac{1}{2}} \tag{5.4}$$

$$\beta = d/D \tag{5.5}$$

and

$$\varepsilon = 1 - (0.41 + 0.35\beta^4)\frac{\Delta p}{\kappa p_1} \tag{5.6}$$

where $\kappa = c_p/c_v$

5.5 Experimental results

The following section covers the results obtained during the experiments. The results as well as comparison and validation of the simulation will be discussed.

5.5.1 Temperature

The heat transfer characteristics are compared by evaluating the temperature increase from the inlet to the outlet of both the experiment and the curved duct simulation.

In Figure 5.4 the experimental results are seen to be about 10 % lower than the simulation results at low flow rates. This is due to the simulation being the ideal situation for such a case, not taking into account any external factors that could play a role. Less losses occur at high flow rates due to the lower operating air temperature. Furthermore, it is seen that the two results are within good correlation to each other at high flow rates and have the same trend.

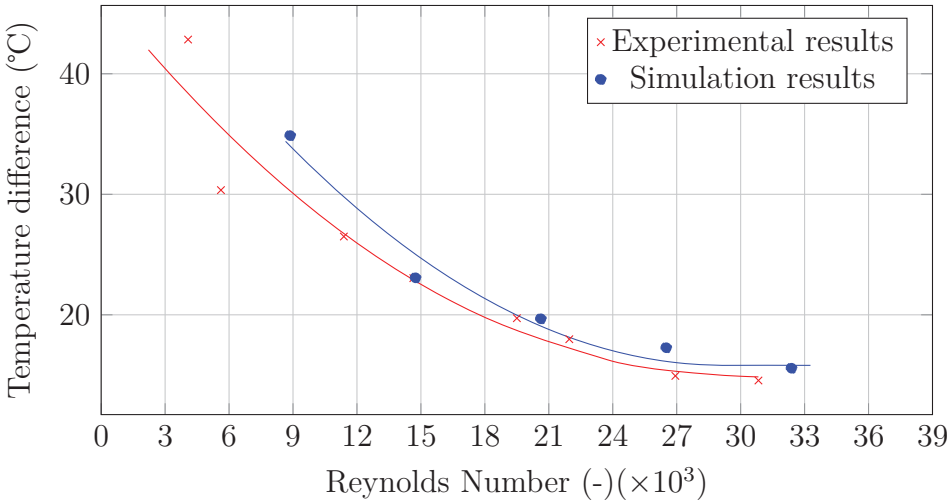

Figure 5.4: Experimental over numerical results for temperature difference at different Reynolds numbers

5.5.2 Pressure drop

There are three pressure taps situated within the heated section of the set-up which measures the differential static pressure to the inlet. This allows for the computation of the static pressure drop along the ducts.

In Figure 5.5 a graph containing both the curved duct simulation and experimental results of the pressure drop are presented. At low flow rates the pressure drop of the simulation is lower than the experimental pressure drop while at higher flow rate the simulation over-predicts the pressure drop. This occurrence could be due to the roughness of the experimental test part. No surface finishing can be applied to the inner curved surface due to its complex geometry, thus it is very rough and influences the flow.

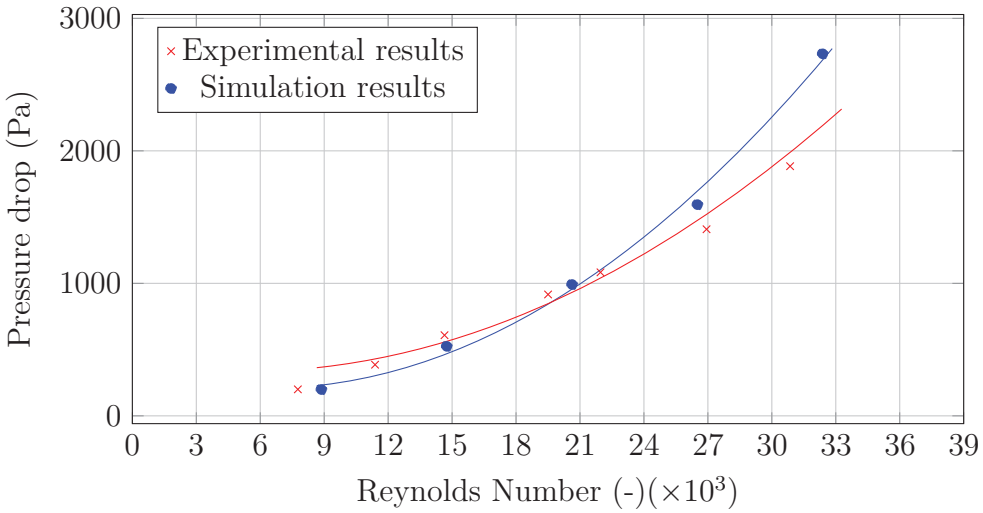

Figure 5.5: Experimental over numerical results for pressure drop at different Reynolds numbers

Chapter 6

Critical comparison of the results

The following section contains an analysis of the analytical, numerical and experimental results. Furthermore, a comparison of the straight duct and the curved duct is done to inspect the predicted increase in heat transfer and pressure drop.

6.1 Heat transfer characteristics

Figure 6.1 contains the relevant heat transfer coefficients, including the theoretical, numerical and experimental results. In this graph some deviation between these three results can be seen. The analytical analysis highly over-predicts the performance of the curved duct while under-predicting the straight duct performance compared to both the numerical and experimental results. The simulation for the curved duct does however show good correlation with that of the experimental results, over-predicting by less than 10 %. This over-prediction could be due to the simulation not accounting for thermal losses in the system, whereas in the experiments they are unavoidable.

The improvement in heat transfer coefficient is not as high as originally expected, having a lower actual improvement (by 25 %) than theoretically predicted in the curved duct and higher (by 12 %) in the case of a straight duct.

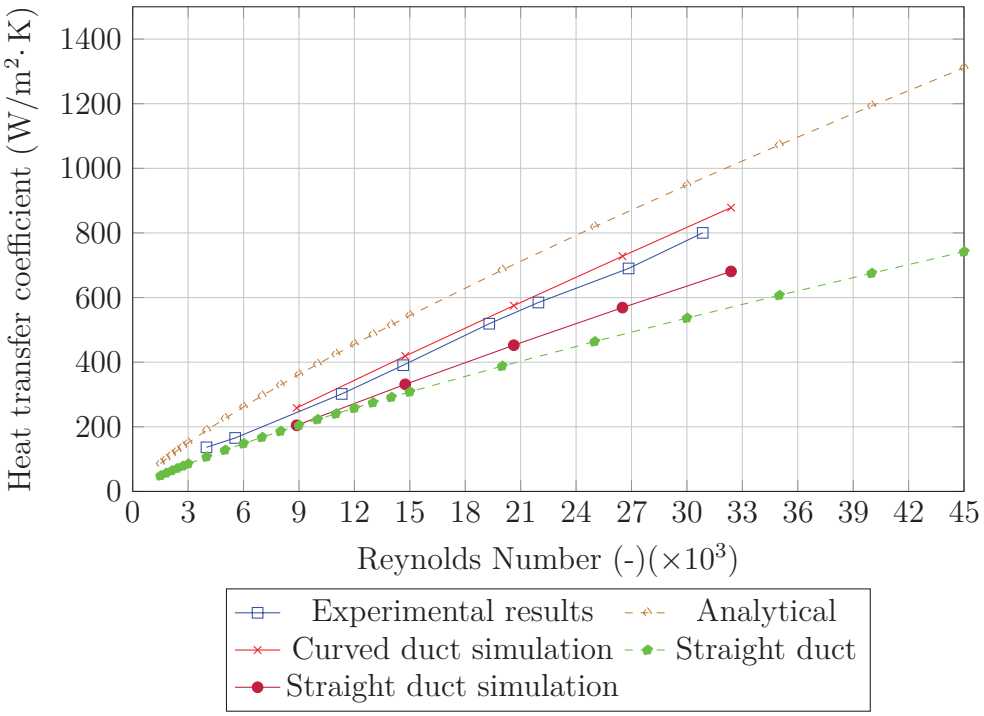

Figure 6.1: Heat transfer over Reynolds number

6.2 Pressure drop

The pressure drop of all the relevant results are presented in Figure 6.2. At low flow rates the analytical results predict the pressure drop well compared to the numerical and experimental results, deviating somewhat at higher flow rates. For the straight duct the theoretical results over-predicts the pressure drop compared to the simulation with a maximum of 10 %, but with less than 4 % on average.

The Kakac and VDI analytical methods results for the curved duct are within 3 % of each other having a slightly different trend line than the curved simulation results. The curved duct simulation under-predicts at low flow rates and over-predicts at higher flow rates. This difference, as previously stated, could be due to a material roughness present during the data gathering for the correlations. The simulation is an ideal situation with no impacting external factors. Further, the theoretical results agree well with the experimental results, slightly over-predicting at higher flow rates but still staying within a 10 % error or less.

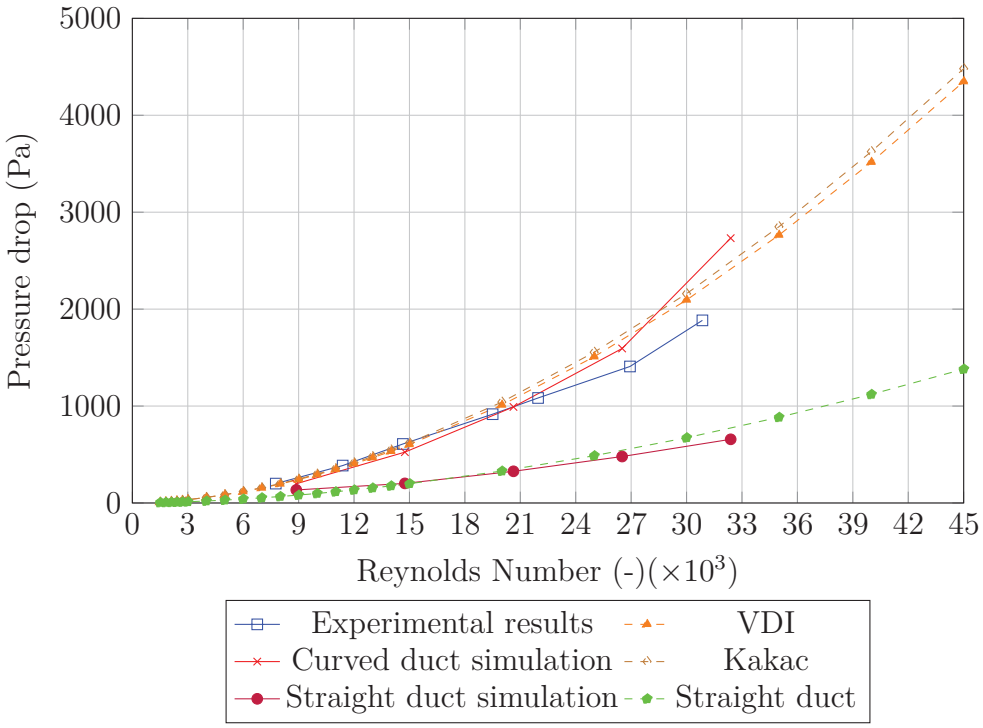

Figure 6.2: Pressure drop over Reynolds number

6.3 Normalised gain

Figure 6.3 shows the normalised gain in heat transfer coefficient divided by the normalised pressure loss over the mass flow rate. This measure of performance shows the maximum flow rate at which the pressure loss (efficiency decrease) will surpass the heat transfer coefficient increase (efficiency increase). Any flow rate higher than this point (0.035 kg/s) will cause the pressure loss increase to exceed the increase experienced by the heat transfer coefficient. The design point flow rate is below this point, where the heat transfer coefficient increase is 23 % and the pressure drop increase is 20 %.

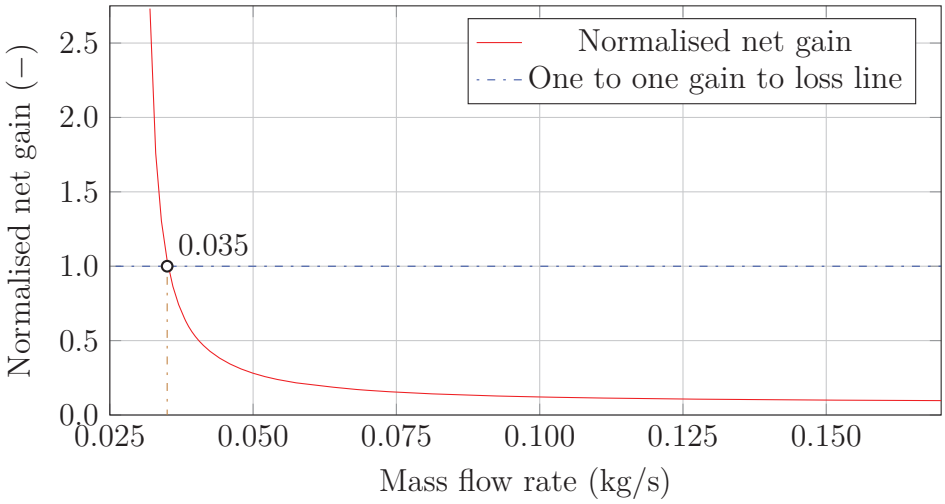

Figure 6.3: Normalised heat transfer gain divided by normalised pressure loss over mass flow rates

Chapter 7

Conclusion

The introduction of a swirl to the SCRAP receiver concept could be a viable solution to improving the heat transfer coefficient.

7.1 Contribution

The first task was to find a desired angle for the helically swirled fins. The test set-up provided a test length of 200 mm. The analytical analysis showed potential for one full rotation, thus it was decided to test a full rotation within the 200 mm test section. These parameters gave an average helix angle is of 36.1°.

The analytical analysis on the curved duct showed good improvement in the heat transfer coefficient compared to the straight duct, with some results showing more than a 100 % improvement at high flow rates and up to 35 % increase at the design point.

The pressure drop was observed to be very large during the initial theoretical analysis, with a pressure drop increase exceeding 150% when implementing the curved duct. The pressure drop increase at the design point was calculated to be 30 %. This was to be further investigated by means of a simulation and experimental process.

The CFD simulations of both the straight and curved duct were designed to be compatible to the test set-up. Table 3.6, in Chapter 3, contains all the numerical results. It is seen that there is a good increase, 25 % on average, in the heat transfer coefficient, but the increase in pressure drop surpasses the increase in heat transfer coefficient at higher flow rates.

A comparison of the theoretical and numerical results exhibits a good correlation in the pressure drop analysis. However, the heat transfer coefficient show

deviations as large as 23 % for both the straight and curved duct simulations. The heat transfer coefficient is not increased, by the curved duct, to the extent that was initially thought, while the heat transfer coefficient for the straight duct is higher than theoretically calculated. This predicts a smaller increase in heat transfer coefficient than what was expected.

Comparing the experimental and numerical results it was found that the pressure drop for the simulation is under-predicted at low flow rates and over-predicted at higher flow rates.

The results of all the findings were analysed in Chapter 6 and represented in Figures 6.1 and 6.2, which shows the analytical, numerical and experimental results. Through analysis the curved duct simulation was validated by the experimental results.

The curved duct simulation over-predicts the heat transfer coefficient results of the experiment with a maximum of just less than 10 %. This maximum over-prediction is present at high flow rates, that being said, the simulation predicts the heat transfer coefficient well at low flow rates. The theoretical results over-predict the actual heat transfer coefficient by 25 %. Furthermore, the straight duct simulation is under-predicted by the theoretical results.

The pressure drop of the curved duct simulation compares well to that of the experimental results, having an average error of 4 % and maximum error of 10 %. Compared to the theoretical results the pressure drop was well predicted for the specific system. The trend line for both the experimental and theoretical line stay within 7 % of each other, having a very small error difference at flow rates of $5000 < \mathrm{Re} < 22\,000$.

Pressure drop in the straight duct simulation are in good agreement with the theoretical results. At Reynolds numbers of $5000 < \mathrm{Re} < 26\,500$ the results stay within 4 % error from each other, deviating somewhat at higher flow rates.

Further, as predicted by theoretical analysis, and proved by the experimental and numerical results, the heat transfer coefficient does improve when implementing a curved duct. After all analyses was done it can be concluded that the curved duct does increase the heat transfer coefficient effectively when not exceeding a flow rate of 0.035 kg/s. A further analysis on the specific power gain and power needed for pressure loss can be conducted to investigate at exactly which flow rate the efficiency decreases.

The design point is below 0.035 kg/s (0.0326 kg/s), which makes the swirled fins a possibility. However, the design of such a fin is complex and the cost of manufacturing is very high. With an increase of 23 % in heat transfer co-

efficient and an increase in pressure drop of 20 %, keeping in mind the cost of manufacturing, the implementation of these swirled fins in a spike is challenging.

7.2 Further work

Simulations with different heat sources, various swirling angles, smaller fins and the effect of fins within the spike tip are some of the possibilities.

7.2.1 Different swirl angle (trade off)

With the implementation of different swirl angles in various simulations the full effect of the swirl can be understood. With the current swirl there is a large pressure drop present with a moderate increase in heat transfer coefficient. A duct with less swirl could decrease the pressure drop adequately without effecting the increase in heat transfer coefficient to a large extent.

7.2.2 Smaller "fins" to disturb flow

Seeing that the pressure drop is a major priority, smaller, thinner fins with a chamfer from the tip, as presented in Figure 7.1, should be investigated. The fins starts thin and then thickens as the distance from the end cap increases. With this change in geometry the air will avoid hitting a major obstacle, thus having a smaller pressure loss. Further, investigating the what the effect would be if the length of the fins increases as the distance from the tip increases could be vital, easing the air flow stream into the fins and once again avoiding major obstacles. The two above mentioned modifications could contribute to decreasing the pressure loss while maintaining the desired heat transfer coefficient increase, making the swirled fins a crucial part of the SCRAP.

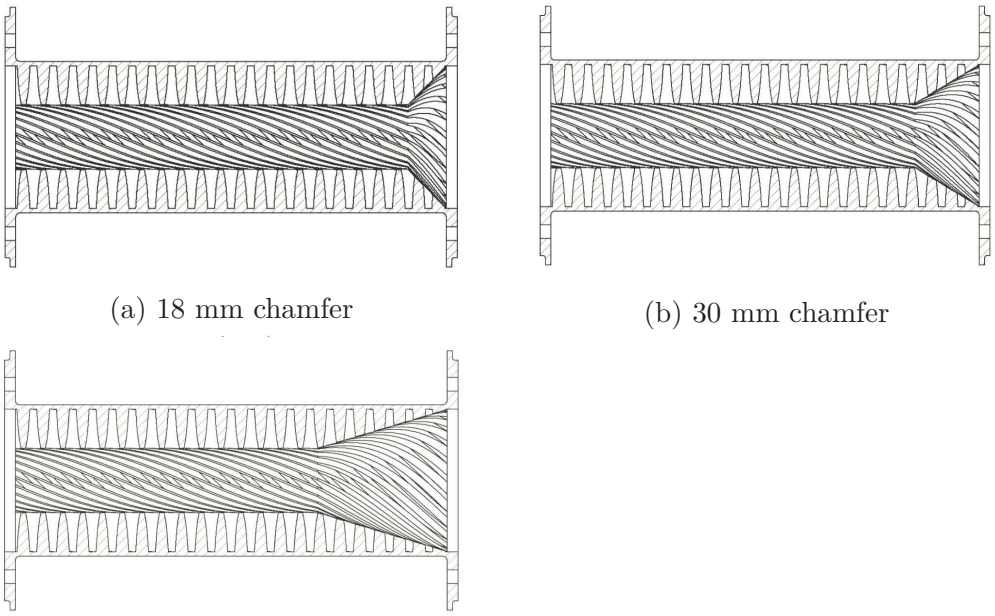

(a) 18 mm chamfer

(b) 30 mm chamfer

(c) 60 mm chamfer

Figure 7.1: Further modified tube

7.2.3 Possibility of fins in tip

The final proposed improvement is fins within the tip. The tip is where the largest amount of heat transfer takes place. Implementing small fins on the inner hemisphere could benefit the heat transfer while not affecting the pressure drop in the system.

Appendices

Appendix A

Grid independence

The mesh independence had for the straight duct simulation had to be proven. Five different meshes were utilised to establish whether there is mesh independence in the curved duct simulation. The meshes were checked in terms of mesh size and the computational time. Two course, one medium and two fine meshes were used, with the fine meshes having up to 1 000 000 and 630 000 cells, the medium mesh 277 000 and the course meshes 165 000 and 80 000. The local wall heat transfer coefficients at the inner and outer flow area were used to investigate and establish the independence. Table A.1 shows the detail of each mesh used during the mesh independence study. A detailed view containing a section of the mesh can be seen in Figure A.1. The mesh down the length of the fluid domain is shown in Figure A.2.

Table A.1: Curved duct simulation mesh details

Mesh nr	Cells $\times 10^3$	Faces $\times 10^3$	Nodes $\times 10^3$
1	80,9	256	938
2	164	516	184
3	277	856	301
4	633	1936	670
5	1035	3153	2083

Figure D.3 show the heat transfer on the inner fluid surface from inlet to the outlet of all the meshes. Seeing that the heat transfer coefficient is the within 1% from each other only the inner wall surface results are shown. A difference of less than 1% is seen between mesh 4 and 5, thus mesh independence is proven. For computational reasons the results of mesh 4 will be used in further discussions. The exact average error difference in the wall heat transfer between all the above mentioned meshes with regard to the finest mesh (mesh 5) is shown in Table A.2.

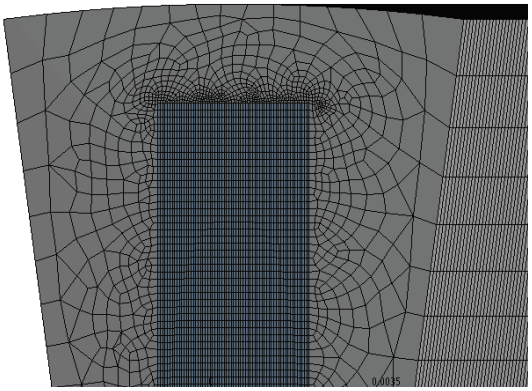

Figure A.1: Partial view of mesh at inlet

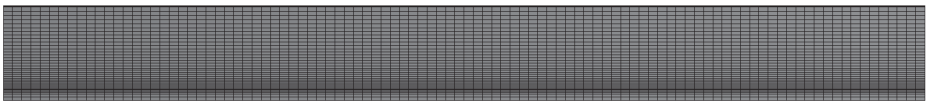

Figure A.2: Detailed view of mesh at inlet

Table A.2: Average error difference in wall heat transfer

Mesh nr	Inner Fluid Surface	Outer Fluid Surface
1	23.1%	22.8%
2	16.5%	16.9%
3	11.7%	10.9%
4	1.53%	0.723%

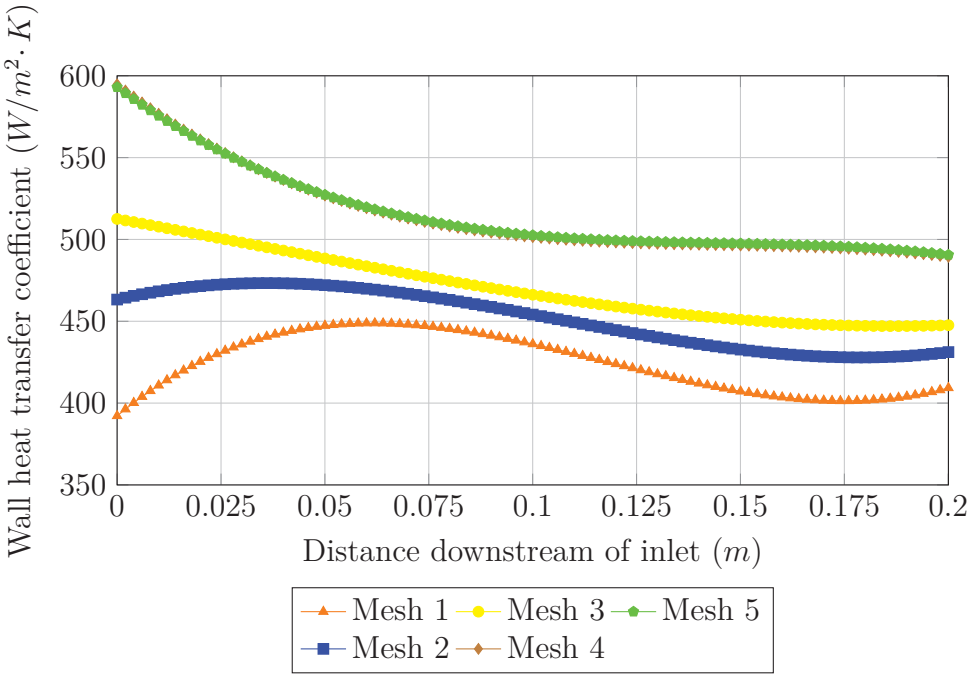

Figure A.3: Heat transfer on the inner fluid surface

Appendix B

Manufacturing and testing of part

B.1 Machining

The test part has a very complex geometry, thus selective laser sintering had to be used to manufacture the part. After this process holes had to be drilled into the fittings to make them interchangeable with the thermocouple and pressure tap fittings. Smaller holes (diameter of 1.6 mm) of different depth were drilled into the thermocouple fitting holes for the thermocouple to slide into. The different depths ranged from 2 mm - 10.4 mm into the fins to increase the quality of data gathered. Further, 0.5 mm holes were drilled through the tube wall for the pressure readings to be possible. Figure B.1 - B.3 shows photos of the test part.

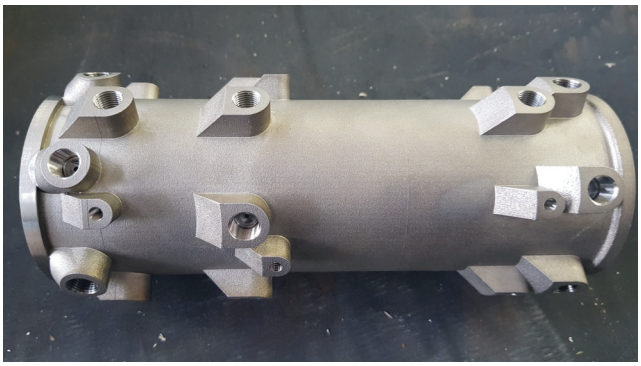

Figure B.1: Test part side view

.

Figure B.2: Test part flanges

.

Figure B.3: Test part front view

.

B.2 Welding

After the machining was done, the flanges had to be welded to the main part. The welding was done with grade 5 (Ti-6Al-4V ELI) titanium rods that had to be special ordered. Figures B.4 - B.6 shows the part after welding and facing of the flanges.

Figure B.4: Test part front view after welding and facing

.

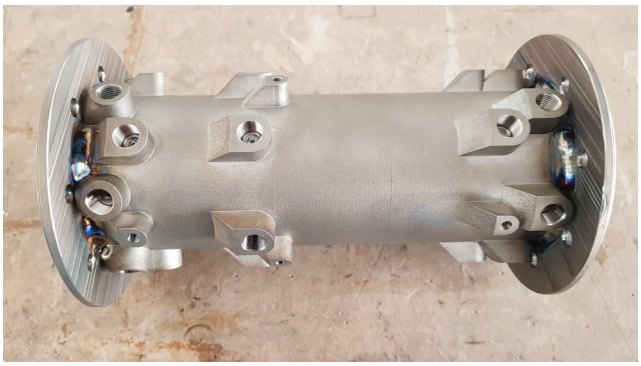

Figure B.5: Test part side vie after welding and facing

.

B.3 Pressure test

A pressure test had to be done to ensure safety while testing. The maximum possible pressure while testing is 10 bar, which is the maximum pressure supplied by the compressor. The part was mounted to a manual water pump system. This system implements a hand pump with a gauge to check the pressure. To ensure the part will not fail under testing a pressure of 14 bar was applied to it. Figures B.6 and B.7 show the mounting system.

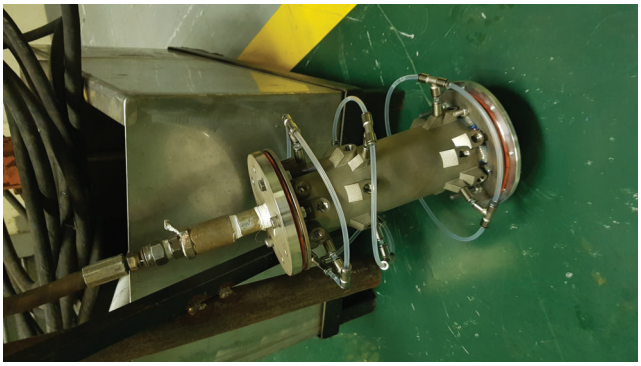

Figure B.6: Manual pressure test system

.

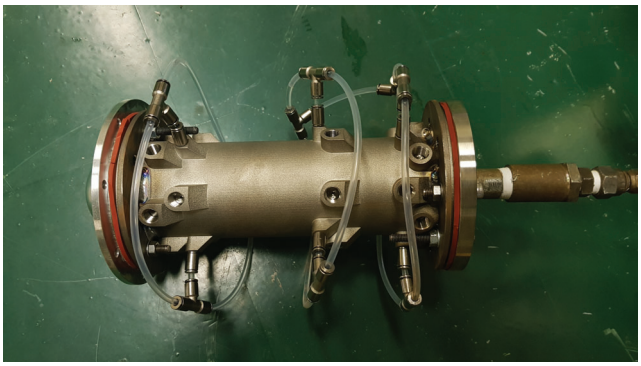

Figure B.7: Mounted test part

.

B.4 Testing

In Figure B.8 the test part is shown connected to the test rig with only pressure tap fitted. Figure B.9 shows the test part connected to the test rig and fully equipped with pressure taps and thermocouples, ready for testing.

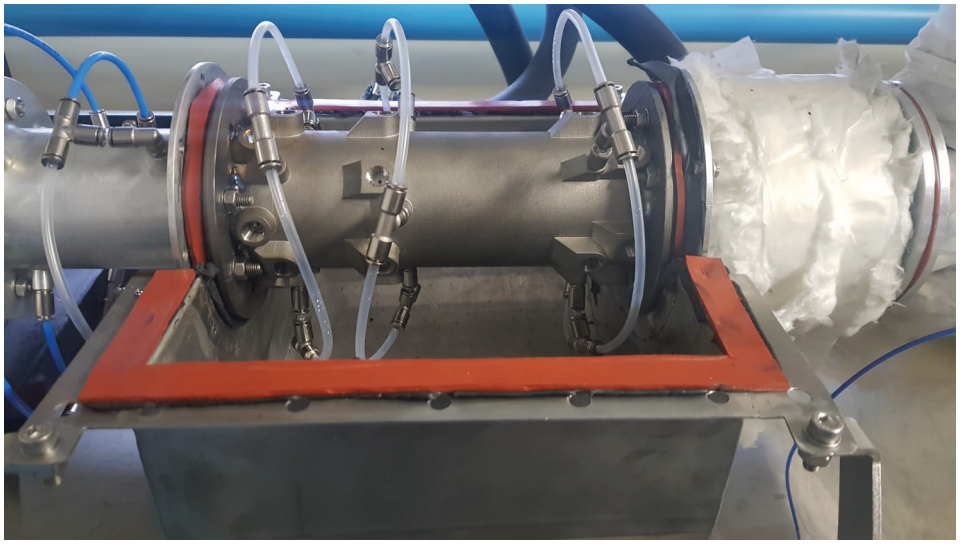

Figure B.8: Test part connected to rig with installed pressure taps

.

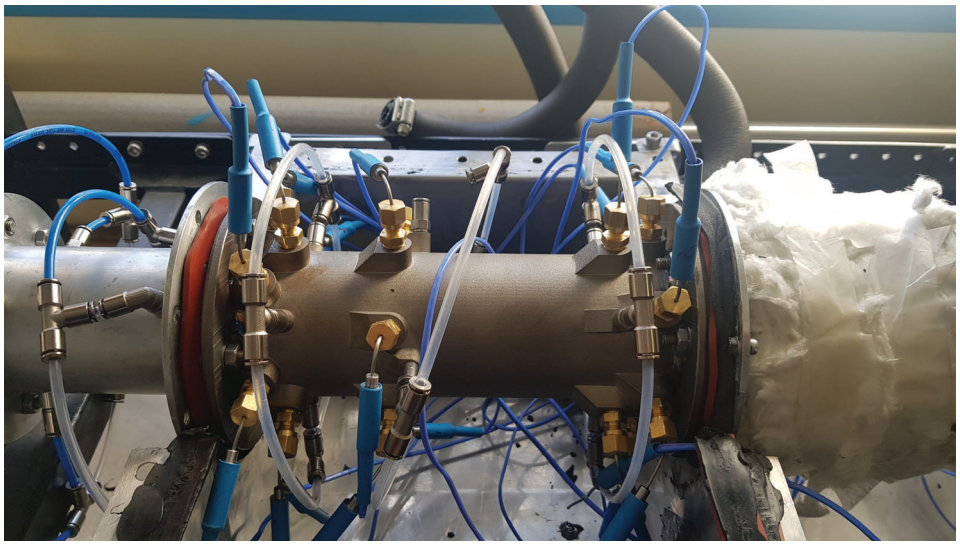

Figure B.9: Fully equipped test part connected to rig

.

Appendix C

Safety procedures

C.1 Introduction

This safety report is for the testing of a SCRAP receiver tube located in the heat transfer lab. The heat transfer rig was made by Dr Lubkoll to model a single spike of the SCRAP design. The test set-up will only be modified by using a different finned section, all other parts remain the same. The test set-up uses steam at 100 °C. The air within the tube operates at a pressure of 10 bar or less and could possibly be heated to the steam temperature. The test system involves no movable parts and operates with non-poisonous and non-flammable gasses. The steam supply is generated by an electrically powered steam generator. The test set-up has no electrical components except for the low voltage pressure regulators and thermocouples.

C.2 Pressure safety of modified design

The test will be executed with a non-dangerous fluid/gas under a temperature of 350 °C. Thus, the specific testing falls under "safe engineering practice" or group II.

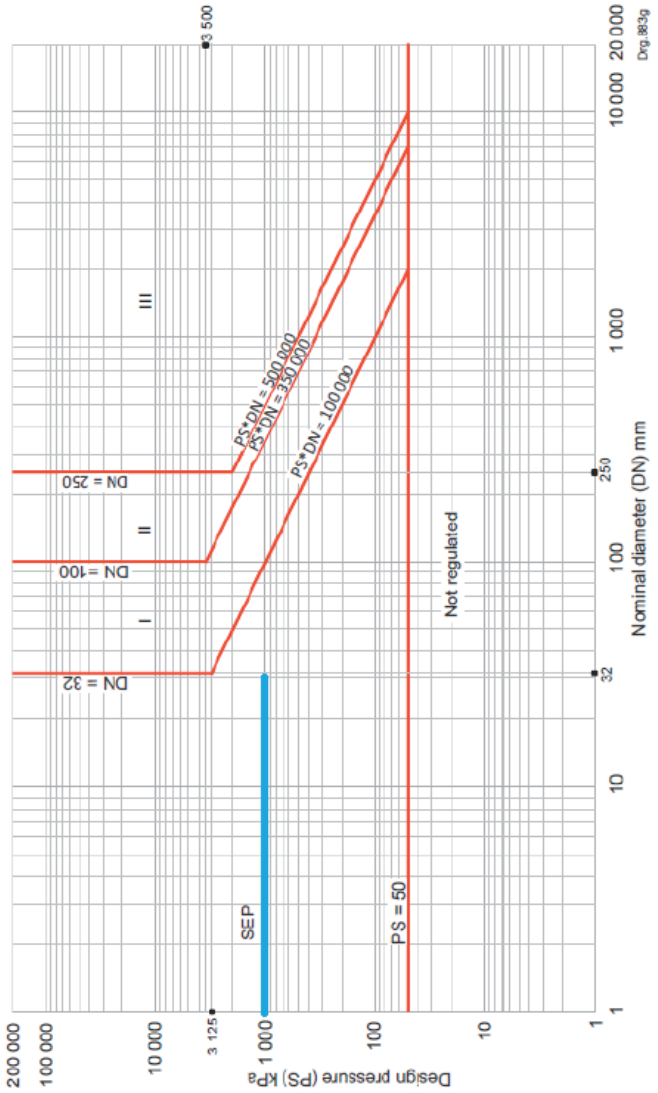

Figure 7 — Graph for piping — Non-dangerous gas

Figure C.1: SANS 347 classification

.

Installation of modified design:

1. Calibrate thermocouples
2. Remove all insulation
3. Remove thermocouples on "old" part
4. Detach two end annulus flow sections
5. Remove current finned test section
6. Install modified test section

7. Attach two end annulus flow sections
8. Seal in between all newly attached and reattached part
9. Attach all pressure taps and thermocouples
10. Enclose steam bath whilst ensuring it is completely sealed
11. Connect the steam and air supple pipes

C.3 Overview of operation

Pressurized air supplied by the 10bar university system enters the set-up. The air is then stopped by an on/off valve followed by a pressure regulator, shown in Figure C.3. The flow regulator controls the flow towards the orifice plate air flow rate test device with two long tube sections to provide fully developed flow. The air then turns 180 degrees and is ducted towards the experimental test section.

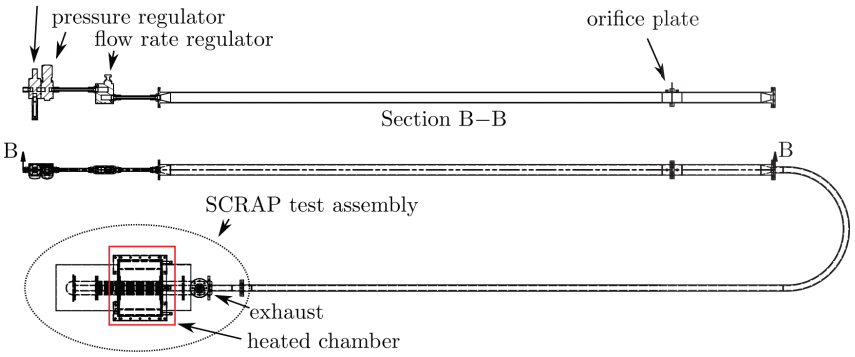

Figure C.2: Test setup

.

The air passes several pressure taps to measure static pressure. The experimental set-up once again returns the air flow 180 degrees and is ducted against the initial air flow direction through an annular space. It is heated from the outside via steam. The steam flows in an open cycle, open to ambient, ensuring no build up pressure. Any unforeseen blockage of steam flow would lead to leakage and pressure release. After the air is heat it exits through a filter and silencer as seen in Figure C.4.
While testing the person conducting the tests will be standing at position 1 shown in Figure C.5. This will be where the laptop is situated thus all readings will be taken from there. The actual test and measurements will be taken at the test zone shown in Figure C.6.

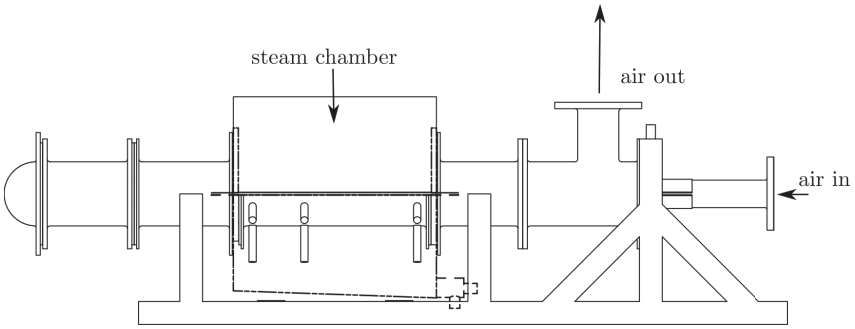

Figure C.3: Experimental section

.

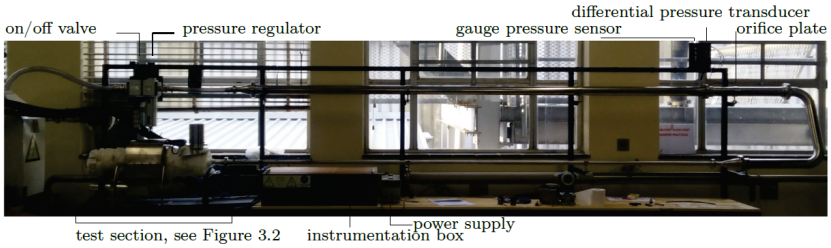

Figure C.4: Safe zone

.

Figure C.5: Test zone

.

Potential Risks

- The system uses pressurized air, this can potentially cause a burst in the tubes.
- The steam exits through a duct where condensate drips from, this may cause exposed heated areas.
- The steam generator may have some hot spots.
- The steam generator could possibly be a noise hazard.

Minimize Risks

- Minimisation of risks against bursting (A FEM analysis of the pressurized air system and adequate design of notches was done by previously done by Matti Lubkoll)
- Minimisation of risks against leakage (Analysis of such locations for leak before burst was done by Matti Lubkoll)
- Test the set-up under 2x maximal operating conditions to ensure test set-up is adequate.
- Minimisation of risk against contact with hot surfaces (The duct steam outlet is place away from accessible areas, warning signs will be placed where needed)
- Safety glasses will be worn during testing
- At least one extra person will be present in the lab while experiments are conducted
- Closed shoes will be worn at all times

Design for Set-up

- The pressurized air can at any time be turned off by means if two on/off valves
- The steam supply can at any time be turned off via the steam generator
- The set-up will be well ventilated in a large laboratory
- A pad lock is in place to lock inlet on/off valve in the off positions while no experiments are being conducted
- The pressurized air is open to ambient via a silencer to ensure the system will always de-pressurize after turning off the inlet pressure
- Keep wiring away from hot surfaces and water

Safety and Operation Conditions
Before conducting experiments:

- Inspect the setup for damage, loose bolts and nuts.
- Inspect all the air piping to ensure no loose fittings.
- Check that the silencer is not clogged by blowing through it.
- Before connecting the steam generator check that piping is not blocked to avoid pressure build-up

- Continuously check the water level of the generator to avoid it from running dry

Beginning experiment:

- Increase pressure and flow rate of the air stream carefully to the desired levels while checking for leakages

During experiments:

- In case of any unusual occurrences steam generator and air supply are to be switched off for investigation
- Inspect steam generators water level during a long test

After experiment:

- Turn off steam generator
- Turn off air supply at main valve
- Lock air supply valve in off position
- Disconnect the steam supply lines

Housekeeping
After each set of experiments

- Lock air supple valve in off position using the pad-lock
- Disconnect steam generator
- And after cooling down, clean tray of all the collected vapor

Appendix D

Calibrations

The calibration for the measuring devices were done to ensure accuracy. The individual calibration curves follow.

D.1 Thermocouples

The thermocouples were calibrated using a thermo-well. A representation of one of the thermocouple's errors before and after calibrations are shown in Figures D1 and D.2. Enough time was given for the temperature to stabilise before a reading was taken. Each thermocouple was calibrated to its own curve.

The raw data was recorded during testing, and only after collecting the data the calibration curves were applied. A higher accuracy could be achieved this way, by applying a curve only fitted to the temperature ranges that the specific thermocouple experienced during testing.

D.2 Pressure transducers and firstrate

Two devices were used for pressure calibrations namely the Betz micromanometer with a range of up to 5000 Pa and a master pressure gauge ranging from 0 - 10 bar. The Betz micromanometer was used for all the pressure transducers while a master gauge was used for the fitsrate calibrations. Increments of 100 kPa were used for the calibration of the firstrate and increments of 500 Pa were used for the pressure transducers. An example of the firstrate is shown in Figure D3 and an example of the pressure transducer calibration is shown in Figure D4.

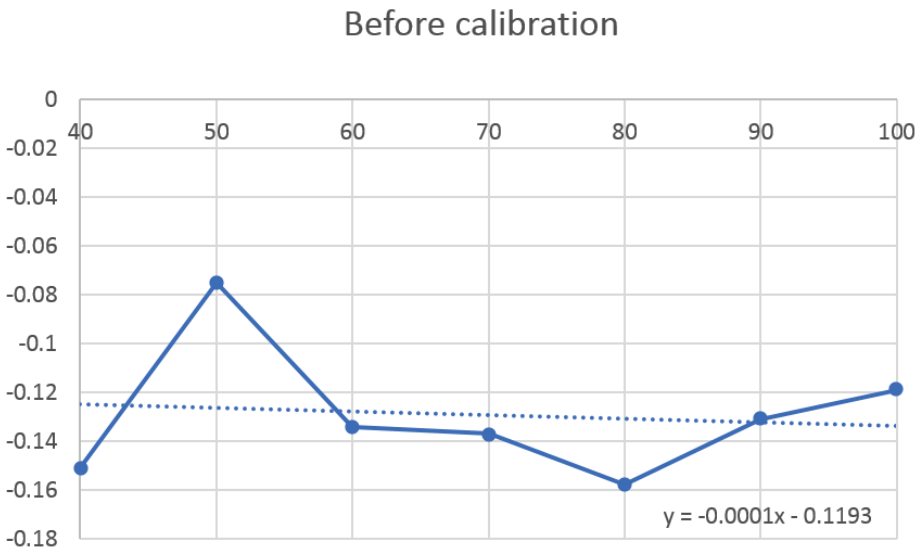

Figure D.1: Thermocouple error before calibration

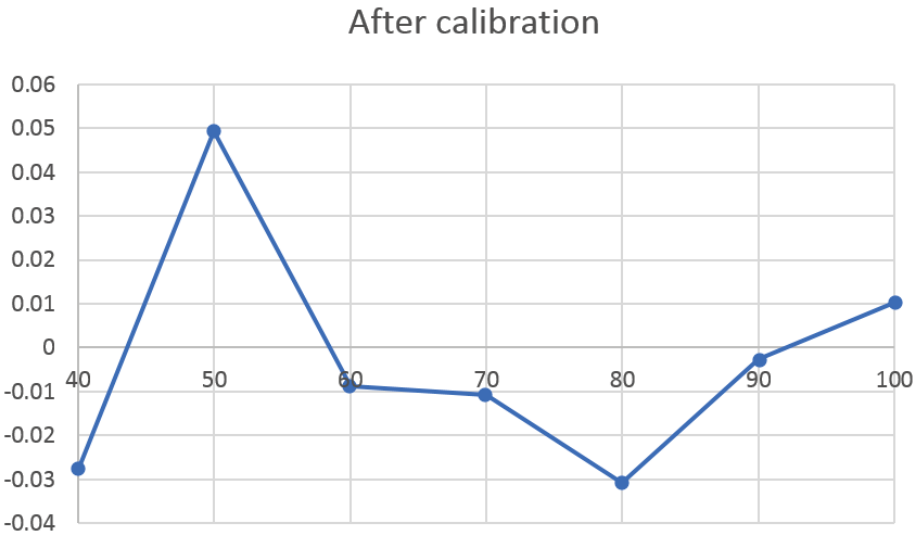

Figure D.2: Thermocouple error after calibration

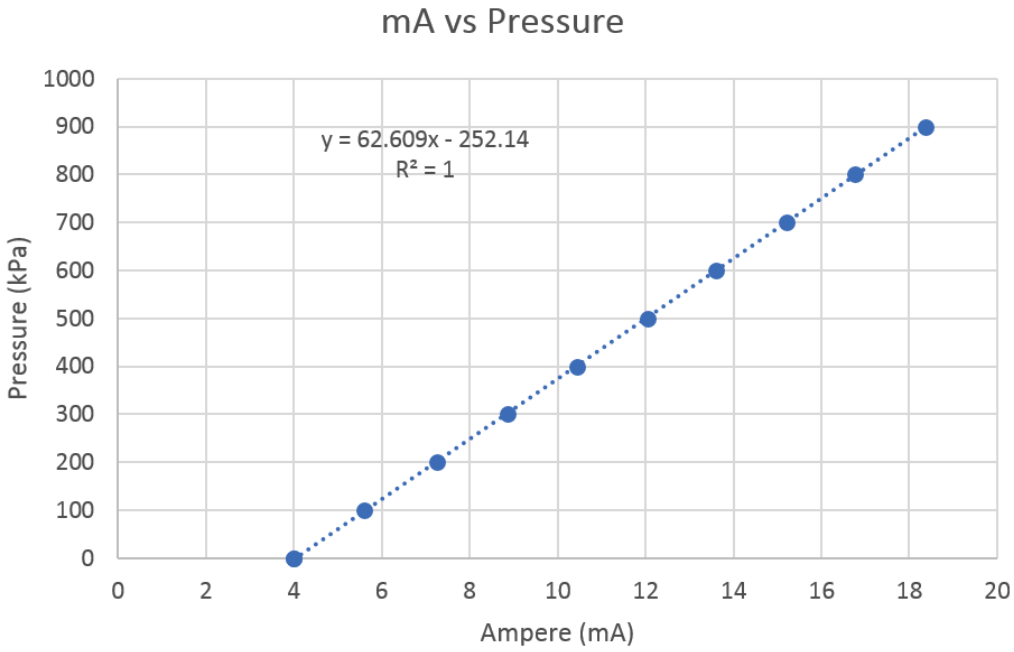

Figure D.3: Fitsrate calibration curve

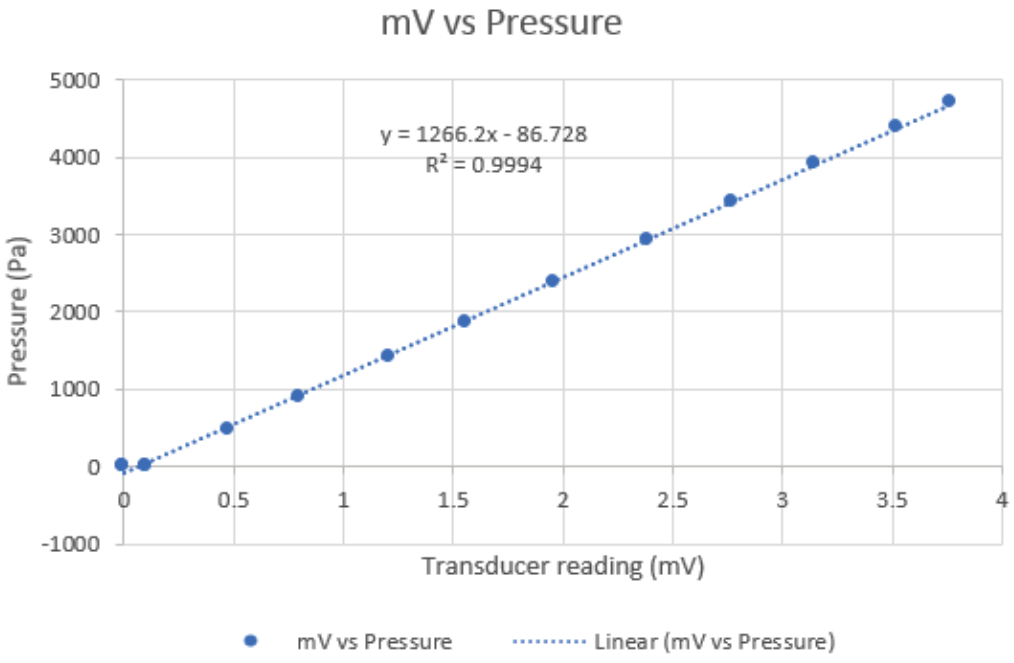

Figure D.4: Pressure transducer calibration curve

List of References

Ali, M.E. (2004). Free convection heat transfer from the outer surface of vertically oriented helical coils in glycerol-water solution. *Heat and Mass Transfer/Waerme Und Stoff Uebertragung*, vol. 40, no. 8, pp. 615–620. ISSN 09477411.

Basse, N.T. (2017). Turbulence Intensity and the Friction Factor for Smooth- and Rough-Wall Pipe Flow. *Fluids*, vol. 2, no. 2, p. 30. ISSN 2311-5521. 1612.08540. Available at: http://www.mdpi.com/2311-5521/2/2/30

Becker, M.A.N.F.R.E.D. (1980). Comparison of Heat Transfer Fluids for Use in Solar Thermal Power Stations *. vol. 3, pp. 139–150.

Boerema, N., Morrison, G., Taylor, R. and Rosengarten, G. (2012). Liquid sodium versus Hitec as a heat transfer fluid in solar thermal central receiver systems. *Solar Energy*, vol. 86, no. 9, pp. 2293–2305. ISSN 0038-092X. Available at: http://dx.doi.org/10.1016/j.solener.2012.05.001

British Standard (1993). *Measurement of Fluid Flow in Closed Conduits*. 1. British Standard Institution, Milton Keynes. ISBN 0580161595.

Cengel, Yunus A. Ghajar, A.J. (2015). *Heat and Mass Transfer*. Fifth edit edn. ISBN 9780073398181.

Chacartegui, R., Sánchez, D., Muñoz, J.M. and Sánchez, T. (2009). Alternative ORC bottoming cycles FOR combined cycle power plants. *Applied Energy*, vol. 86, no. 10, pp. 2162–2170. ISSN 03062619. Available at: http://dx.doi.org/10.1016/j.apenergy.2009.02.016

Chandratilleke, T.T. and Nadim, N. (2014). Secondary flow vortex structures and forced convection heat transfer in fluid flow through curved elliptical ducts. *Proceedings of the Institution of Mechanical Engineers, Part A: Journal of Power and Energy*, vol. 228, no. 5, pp. 550–562. ISSN 20412967.

Chen, H., Goswami, D.Y. and Stefanakos, E.K. (2010). A review of thermodynamic cycles and working fluids for the conversion of low-grade heat. *Renewable and Sustainable Energy Reviews*, vol. 14, no. 9, pp. 3059–3067. ISSN 13640321. Available at: http://dx.doi.org/10.1016/j.rser.2010.07.006

Coronella, C.J. (2008). *Handbook of Heat Transfer Calculations*, vol. 99. ISBN 0070535558.

Dean, W. (1928). Fluid Motion in a Curved Channel. vol. 121, pp. 402–420.

DLR (2010). *Solar-Hybrid Power and Cogeneration Plants, Technical Report 019830, Deutsches Zentrum fur Luft- und Raumfahrt e.V.*

Dostal, V., Hejzlar, P. and Michael J, D. (2006). The Supercritical Carbon Dioxide Power Cycle: Comparison to Other Advanced Power Cycles. *Nuclear Technology*, vol. 154:283-30.

Dow Chemical Company (2001) (). *Synthetic Organic Heat Transfer Fluid Liquid and Vapor Phase Data.*

Duffie, J.a., Beckman, W.a. and Worek, W.M. (2003). *Solar Engineering of Thermal Processes, 4nd ed.*, vol. 116. ISBN 1118418123. arXiv:1011.1669v3. Available at: http://books.google.com/books?hl=en{&}lr={&}id=qkaWBrOuAEgC{&}pgis=1

Dunham, M.T. and Iverson, B.D. (2014). High-ef fi ciency thermodynamic power cycles for concentrated solar power systems. *Renewable and Sustainable Energy Reviews*, vol. 30, pp. 758–770. ISSN 1364-0321.
Available at: http://dx.doi.org/10.1016/j.rser.2013.11.010

Dunham, M.T. and Lipiński, W. (2013). Thermodynamic Analyses of Single Brayton and Combined Brayton-Rankine Cycles for Distributed Solar Thermal Power Generation. *Journal of Solar Energy Engineering*, vol. 135, no. 3, p. 031008. ISSN 0199-6231.

Dunn, B.R.I., Hearps, P.J. and Wright, M.N. (2012). Molten-Salt Power Towers : Newly Commercial Concentrating Solar Storage. vol. 100, no. 2.

European Commission (2005). *SOLGATE, Solar hybrid gas turbine electric power system.* ISBN 9289445920.

Forsberg, C.W., Peterson, P.F. and Zhao, H. (2007). High-Temperature Liquid-Fluoride-Salt Closed-Brayton-Cycle Solar Power Towers. *Journal of Solar Energy Engineering*, vol. 129, no. 2, p. 141. ISSN 01996231.

Freescale (2008). *Freescale Semiconductor MPX2050.* Freescale semiconductor Tempe.

Garbrecht, O. and Kneer, R. (2012). Numerical investigation of a new molten salt central receiver design. , no. September.

Ghobadi, M. and Muzychka, Y.S. (2016). A Review of Heat Transfer and Pressure Drop Correlations for Laminar Flow in Curved Circular Ducts. *Heat Transfer Engineering*, vol. 37, no. 10, pp. 815–839. ISSN 15210537.

Guo, L., Feng, Z. and Chen, X. (2001). An experimental investigation of the frictional pressure drop of steam-water two-phase flow in helical coils. *International Journal of Heat and Mass Transfer*, vol. 44, no. 14, pp. 2601–2610. ISSN 00179310.

Iverson, B.D., Conboy, T.M., Pasch, J.J. and Kruizenga, A.M. (2013). Supercritical CO2Brayton cycles for solar-thermal energy. *Applied Energy*, vol. 111, pp. 957–970. ISSN 03062619.
Available at: `http://dx.doi.org/10.1016/j.apenergy.2013.06.020`

Kakac, S., Shah, R.K. and Aung, W. (1987). *Handbook of single-phase convective heat transfer*. John Wiley & Sons, Inc, Coral Gables, Florida. ISBN 0-471-81702-3.

Kaya, O. and Teke, I. (2005). Turbulent forced convection in helically coiled square duct with one uniform temperature and three adiabatic walls. *Heat and Mass Transfer*, vol. 2, no. 42, pp. 129–139.

Keysight Technologies (2014). *Keysight 34970A Data Acquisition / Switch Unit Family*. Keysight Technologies.

Klimas, P.C. and Becker, M. (1991). Status of second-generation central receiver technologies. *Solar Energy Materials*, vol. 24, no. 1-4, pp. 162–171. ISSN 01651633.

Kröger, D.G. (2008). Spiky Central Receiver Air Pre-heater (SCRAP). Tech. Rep., University of Stellenbosch, Stellenbosch.

Kröger, D.G. (2012). SUNSPOT - Stellenbosch UNiversity Solar Power Thermodynamic cycle. Tech. Rep., University of Stellenbosch, Stellenbosch.

Lata, J.M. (2018). High Flux Central Receivers of Molten Salts for the New Generation of Commercial Stand-Alone Solar Power Plants. vol. 130, no. May 2008, pp. 1–5.

Ligrani, P.M. (1994). A study of Dean vortex development and structure in a curved rectangular channel with aspect ratio of 40 at Dean numbers up to 430. , no. C.

Lubkoll, M. (2017). *Performance Characteristics of the Spiky Central Receiver Air Pre-heater (SCRAP)*. Ph.D. thesis, University of Stellenbosch, Stellenbosch.

Lubkoll, M., Harms, T.M. and Von Backström, T.W. (2016). Introduction to heat transfer test setup and manufacturing process for the SCRAP receiver. In: *4th Southern African Solar Energy Conference*.

Lubkoll, M., Harms, T.M. and Von Backström, T.W. (2017). Introduction to heat transfer test setup for the SCRAP receiver. In: *AIP Conference Proceedings*.

Mancini, T.R., Gary, J.A., Kolb, G.J. and Ho, C.K. (2011). Power Tower Technology Roadmap and cost reduction plan. , no. April. ISSN 9781620814239.
Available at: `http://www.osti.gov/servlets/purl/1011644-0d5QFT/`

McGovern, R.K. and Smith, W.J. (2012). Optimal concentration and temperatures of solar thermal power plants. *Energy Conversion and Management*, vol. 60, pp. 226–232. ISSN 01968904.
Available at: `http://dx.doi.org/10.1016/j.enconman.2011.11.032`

Mori, Y., Uchida, Y. and Ukon, T. (1970). Forced ˜ U ˜ E ˜˜ Curved Channel Heat Transfer in a With a Square Cross Section.

NREL (2013a) (). *Concentrating Solar Power Projects*.

Pacheco, J.E. and Dunkin, S.R. (1996). Assessement of molten-salt solar central-receiver freeze-up and recovery systems.

Pacheco, J.E., Moursund, C., Rogers, D. and Wasyluk, D. (2011). Conceptual design of a 100 MWe modular molten salt. *SolarPACES 2011*, pp. 1–8.
Available at: `http://www.osti.gov/scitech/servlets/purl/1025891`

Paper, T.W., Concept, D., East, M., Africa, N. and Paper, W. (2003). *Clean Power from Deserts EU-MENA*. ISBN 9783929118674.

Petukhov, B. (1970). Heat Transfer and Friction in Turbulent Pipe Flow with Variable Physical Properties. *Advances in Heat Transfer*, vol. 6, pp. 503–564. ISSN 00652717.
Available at: `http://www.sciencedirect.com/science/article/pii/S0065271708701539`

Pitz-paal, R., Giuliano, S. and Wittmann, M. (2015). Concepts for Cost Reduction in CSP Power Plants. In: *DPG Frühjahrstagung 2015*.

Popoola, O. and Cao, Y. (2016). The influence of turbulence models on the accuracy of CFD analysis of a reciprocating mechanism driven heat loop. *Case Studies in Thermal Engineering*, vol. 8, pp. 277–290. ISSN 2214157X.
Available at: `http://dx.doi.org/10.1016/j.csite.2016.08.009`

Price, H., Lupfert, E., Kearney, D., Zarza, E., Cohen, G., Gee, R. and Mahoney, R. (2002). Advances in Parabolic Trough Solar Power Technology. *Journal of Solar Energy Engineering*, vol. 124, no. 2, pp. 109–125. ISSN 01996231.

Santana, D. (2013). Thermal , mechanical and hydrodynamic analysis to optimize the design of molten salt central receivers of solar tower power plants . Key words. vol. 1, no. 11.

Schwarzbözl, P., Buck, R., Sugarmen, C., Ring, A., Marcos Crespo, M.J., Altwegg, P. and Enrile, J. (2006). Solar gas turbine systems: Design, cost and perspectives. *Solar Energy*, vol. 80, no. 10, pp. 1231–1240. ISSN 0038092X.

Shih, T.-H., Liou, W.W., Shabbir, A., Yang, Z. and Zhu, J. (1995). A new k-epsilon eddy viscosity model for high Reynolds number turbulent flows. *Compurers Fluids*, vol. 24, no. 3, pp. 227–238. ISSN 00457930. `NIHMS150003`.

Sleiti, A.K. (2011). Heat transfer and pressure drop through rectangular helical ducts. *Journal of Renewable and Sustainable Energy*, vol. 3, no. 4. ISSN 19417012.

Sofu, T., Chun, T.-H., In, W.-K. and P. Tzanos, C. (2004). Evaluation of turbulence models for flow and heat transfer in fuel rod bundle geometries. *The Physics of Fuel Cycles and Advanced Nuclear Systems: Global Developments*.

Soong, C. and Yan, W. (1999). Development of secondary flow and convective heat transfer in isothermal / iso-flux rectangular ducts rotating about a parallel axis. *International Journal of heat and mass transfer*, vol. 42, pp. 497–510.

Stephan, P., Martin, H., Kabelac, S. and Mewes, D. (2010). *VDI Heat Atlas*. VDI-Verlag GmbH, Düsseldorf. ISBN 9783540778769.

Stine, W.B. and Geyer, M. (2001). Power from the sun.
Available at: `http://www.powerfromthesun.net/book.html`

Wasserman, S. (2016). Choosing the Right Turbulence Model for Your CFD Simulation.

Weniger, J., Tjaden, T. and Quaschning, V. (2014). Sizing of residential PV battery systems. *Energy Procedia*, vol. 46, pp. 78–87. ISSN 18766102.

Wu, S.Y., Chen, S.J., Li, Y.R. and Li, L.J. (2009). Numerical investigation of turbulent flow, heat transfer and entropy generation in a helical coiled tube with larger curvature ratio. *Heat and Mass Transfer/Waerme- und Stoffuebertragung*, vol. 45, no. 5, pp. 569–578. ISSN 09477411.

Xin, R.C. and Ebadian, M.A. (1997). The Effect of Prandtl Numbers on Local and Average Convective Heat Transfer Characteristics in Helical Pipes. *ASME J. Heat Transfer*, vol. 119, no. 3, pp. 467–473.

Xing, Y., Zhong, F. and Zhang, X. (2014). Numerical Study of Turbulent Flow and Convective Heat Transfer Characteristics in Helical Rectangular Ducts. *Journal of Heat Transfer*, vol. 136, no. 12, p. 121701. ISSN 0022-1481.

Yang, M., Yang, X., Yang, X. and Ding, J. (2010). Heat transfer enhancement and performance of the molten salt receiver of a solar power tower. *Applied Energy*, vol. 87, no. 9, pp. 2808–2811. ISSN 0306-2619.
Available at: `http://dx.doi.org/10.1016/j.apenergy.2009.04.042`